Intermediate-mass black holes in dwarf galaxies out to redshift ∼2.4 in the Chandra COSMOS-Legacy Survey

M. Mezcua, F. Civano, S. Marchesi, H. Suh, G. Fabbiano, M. Volonteri

Monthly Notices
of the
ROYAL ASTRONOMICAL SOCIETY

MNRAS **478,** 2576–2591 (2018)
Advance Access publication 2018 May 4

doi:10.1093/mnras/sty1163

Intermediate-mass black holes in dwarf galaxies out to redshift ∼2.4 in the *Chandra* COSMOS-Legacy Survey

M. Mezcua,[1,2]★ F. Civano,[3] S. Marchesi,[4] H. Suh,[5,6] G. Fabbiano[3] and M. Volonteri[7]

[1]*Institute of Space Sciences (ICE, CSIC), Campus UAB, Carrer de Magrans, E-08193 Barcelona, Spain*
[2]*Institut d'Estudis Espacials de Catalunya (IEEC), Carrer Gran Capità, E-08034 Barcelona, Spain*
[3]*Harvard-Smithsonian Center for Astrophysics (CfA), 60 Garden Street, Cambridge, MA 02138, USA*
[4]*Department of Physics & Astronomy, Clemson University, Clemson, SC 29634, USA*
[5]*Institute for Astronomy, University of Hawaii at Manoa, 2680 Woodlawn Drive, Honolulu, HI 96822, USA*
[6]*Subaru Telescope, National Astronomical Observatory of Japan, 650 North A'ohoku Place, Hilo, HI 96720, USA*
[7]*Institut d'Astrophysique de Paris, UPMC et CNRS, UMR 7095, 98 bis bd Arago, F-75014 Paris, France*

Accepted 2018 April 29. Received 2018 April 19; in original form 2017 July 24

ABSTRACT

We present a sample of 40 active galactic nucleus (AGN) in dwarf galaxies at redshifts $z \lesssim 2.4$. The galaxies are drawn from the *Chandra* COSMOS-Legacy survey as having stellar masses $10^7 \leq M_* \leq 3 \times 10^9$ M$_\odot$. Most of the dwarf galaxies are star forming. After removing the contribution from star formation to the X-ray emission, the AGN luminosities of the 40 dwarf galaxies are in the range $L_{0.5-10\,\mathrm{keV}} \sim 10^{39}-10^{44}$ erg s^{-1}. With 12 sources at $z > 0.5$, our sample constitutes the highest-redshift discovery of AGN in dwarf galaxies. The record-holder is cid_1192, at $z = 2.39$ and with $L_{0.5-10\,\mathrm{keV}} \sim 10^{44}$ erg s^{-1}. One of the dwarf galaxies has $M_* = 6.6 \times 10^7$ M$_\odot$ and is the least massive galaxy found so far to host an AGN. All the AGN are of type 2 and consistent with hosting intermediate-mass black holes (BHs) with masses ∼10^4–10^5 M$_\odot$ and typical Eddington ratios >1 per cent. We also study the evolution, corrected for completeness, of AGN fraction with stellar mass, X-ray luminosity, and redshift in dwarf galaxies out to $z = 0.7$. We find that the AGN fraction for $10^9 < M_* \leq 3 \times 10^9$ M$_\odot$ and $L_\mathrm{X} \sim 10^{41}$–$10^{42}$ erg s^{-1} is ∼0.4 per cent for $z \leq 0.3$ and that it decreases with X-ray luminosity and decreasing stellar mass. Unlike massive galaxies, the AGN fraction seems to decrease with redshift, suggesting that AGN in dwarf galaxies evolve differently than those in high-mass galaxies. Mindful of potential caveats, the results seem to favour a direct collapse formation mechanism for the seed BHs in the early Universe.

Key words: galaxies: active – galaxies: dwarf – galaxies: starburst – X-rays: galaxies.

1 INTRODUCTION

Supermassive black holes (SMBHs) reside at the centre of most local massive galaxies (see reviews by Kormendy & Ho 2013; McConnell & Ma 2013) and power the most luminous quasars observed at $z \sim 7$ (e.g. Fan et al. 2003; Willott et al. 2007; Mortlock et al. 2011; Venemans et al. 2013; Wu et al. 2015); however, how these massive BHs form is not clearly understood. The existence of seed black holes (BHs) of $100 < M_\mathrm{BH} < 10^6$ M$_\odot$ [or intermediate-mass BHs (IMBHs)] at $z > 10$ has been invoked in order to explain the finding of SMBHs when the Universe was less than 1 Gyr old (e.g. see reviews by Volonteri 2010, 2012; Greene 2012; Reines & Comastri 2016; Mezcua 2017). Such seed BHs could form from the death of the first generation of (Population III) stars (e.g. Bromm & Larson 2004), from direct collapse of inflowing dense gas in protogalaxies (e.g. Loeb & Rasio 1994; Lodato & Natarajan 2006), or from mergers in dense stellar clusters (e.g. Portegies Zwart et al. 1999; Devecchi & Volonteri 2009; Mapelli 2016) and then grow via accretion and mergers to reach the 10^9 M$_\odot$ of the high-z SMBHs in less than 1 Gyr (e.g. Natarajan 2014; Johnson & Haardt 2016). Alternatively, SMBHs at $z \sim 5-6$ could directly form by mergers of protogalaxies (e.g. Mayer et al. 2010, 2015; but see Ferrara, Haardt & Salvaterra 2013).

The presence of IMBHs at $z > 7$ is difficult to prove (e.g. Sobral et al. 2015; Agarwal et al. 2016; Pacucci et al. 2016; Smith, Bromm & Loeb 2016; Pezzulli et al. 2017b); however, observational evidence for their existence can be found in the local Universe as those 'leftover' seed BHs from the early Universe that did not grow into SMBHs (e.g. see review by Mezcua 2017). The first IMBHs were suggested in globular clusters, where several candidates have been found and stringent BH mass upper limits have been provided

★ E-mail: marmezcua.astro@gmail.com

(e.g. Maccarone, Fender & Tzioumis 2005; Strader et al. 2012; Lützgendorf et al. 2011, 2012, 2013; Feldmeier et al. 2013; Haggard et al. 2013; Leigh et al. 2014; Wrobel, Nyland & Miller-Jones 2015; Wrobel, Miller-Jones & Middleton 2016; Kızıltan, Baumgardt & Loeb 2017), and to explain those ultraluminous X-ray sources (ULXs) with X-ray luminosities above 5×10^{40} erg s^{-1}, which are not easy to explain by stellar-mass BHs even when invoking super-Eddington accretion (e.g. Farrell et al. 2009; Sutton et al. 2012; Mezcua et al. 2013b, 2015; Heida, Jonker & Torres 2015). The three strongest IMBH candidates among ULXs have jet radio emission spatially coincident with the X-ray emission and are most likely the stripped nucleus of a dwarf galaxy undergoing a minor merger event with the ULX host galaxy (e.g. Webb et al. 2010, 2017; Farrell et al. 2012; Mapelli, Zampieri & Mayer 2012; Soria, Hau & Pakull 2013; Kim et al. 2015; Mezcua et al. 2015; Kim, Ho & Im 2017). The nuclei of dwarf galaxies are among the best places where to look for the leftover seed BHs, as dwarf galaxies have not significantly grown through merger and accretion processes and thus resemble the first galaxies that populated the early Universe.

The search for low-mass BHs ($M_{\rm BH} \lesssim 10^6$ M$_\odot$) in dwarf galaxies is mostly based on the detection of X-ray emission (e.g. Greene & Ho 2007a; Desroches, Greene & Ho 2009; Reines et al. 2011; Dong et al. 2012; Schramm et al. 2013; Baldassare et al. 2015, 2017; Lemons et al. 2015; Secrest et al. 2015; Pardo et al. 2016; Chen et al. 2017), in some cases spatially coincident with jet radio emission (e.g. Reines et al. 2014; Nucita et al. 2017), or the use of standard virial techniques to estimate the BH mass (e.g. Barth et al. 2004; Greene & Ho 2004, 2007b; Peterson et al. 2005; Reines, Greene & Geha 2013; La Franca et al. 2015; Bentz et al. 2016; Onori et al. 2017; Liu et al. 2018; Chilingarian et al. 2018; see Mezcua 2017 for a review). Additional searches in the infrared (IR) regime have yielded a few more candidates (e.g. Satyapal et al. 2007, 2008, 2009, 2014; Sartori et al. 2015; Marleau et al. 2017). Most of these samples are however incomplete, very local ($z < 0.3$), skewed towards high Eddington ratios, or skewed towards type-1 active galactic nucleus (AGN) in the case of optical searches (e.g. Greene & Ho 2004, 2007b; Reines et al. 2013) which can hamper the detection of BHs lighter than 10^5 M$_\odot$ if the size of the broad-line region is controlled by BH mass (e.g. Chakravorty, Elvis & Ferland 2014). Baldassare et al. (2015) found an AGN with $M_{\rm BH} \sim 5 \times 10^4$ M$_\odot$ estimated using the virial technique, Yuan et al. (2014) performed a study of four low Eddington ratio sources, and Pardo et al. (2016) searched for AGN in dwarf galaxies out to $z < 1$. Yet, these studies include very few sources. To circumvent the biases mentioned above, in Mezcua et al. (2016) we performed an X-ray stacking analysis of ∼50 000 dwarf galaxies selected in the COSMOS field making use of the recently completed *Chandra* COSMOS-Legacy survey (Civano et al. 2016). We found that a population of IMBHs with X-ray luminosities $\sim 10^{39}-10^{40}$ erg s^{-1} does exist in dwarf galaxies out to $z = 1.5$ and that their detection beyond the local Universe is most likely hampered by their low luminosity and mild obscuration unless deep surveys like the *Chandra* COSMOS-Legacy are used.

The *Chandra* COSMOS-Legacy survey is a combination of the C-COSMOS survey (1.8 Ms, Elvis et al. 2009) with 2.8 Ms of new *Chandra* observations, thus covering a total of 2.2 deg^2 with a exposure time of 4.6 Ms. Nearly all the X-ray sources in the *Chandra* COSMOS-Legacy survey have optical and near-IR counterparts (Marchesi et al. 2016a) from *Hubble*, *Spitzer*, Subaru, Canada-France-Hawaii Telescope, Magellan, VLT, or VISTA observations and the field has been additionally covered by *Herschel*, *GALEX*, *XMM–Newton*, *NuSTAR*, and the VLA. The COSMOS survey constitutes thus the largest survey with a complete, deep ($i_{\rm AB} \sim 27$), multiwavelength data set.

In this paper, we make use of the large area covered and the depth of COSMOS-Legacy to investigate the presence of accreting BHs in dwarf galaxies with stellar masses $10^7 \leq M_* \leq 3 \times 10^9$ M$_\odot$ (i.e. comparable or less massive than the Large Magellanic Cloud) beyond the local Universe. We find a total of 40 dwarf galaxies out to $z = 2.4$ hosting AGN of type 2, with a wide range of accreting rates (from sub-Eddington to super-Eddington accretion) and BH masses consistent with IMBHs. This constitutes the largest sample of IMBHs beyond the nearby Universe, circumventing the biases of previous samples, and allows us to study the fraction of AGN in dwarf galaxies and its evolution with redshift, X-ray luminosity and stellar mass down to X-ray luminosities of $\sim 10^{41}$ erg s^{-1} and $z = 0.7$. The sample and X-ray analysis are presented in Section 2, while the results obtained are reported and discussed in Section 3. Final conclusions are provided in Section 4. Throughout the paper, we adopt a ΛCDM (Λ cold dark matter) cosmology with parameters $H_0 = 70$ km s^{-1} Mpc^{-1}, $\Omega_\Lambda = 0.73$, and $\Omega_m = 0.27$.

2 SAMPLE AND ANALYSIS

The sample of dwarf galaxies is drawn from a parent sample of ∼2300 X-ray-selected type-2 AGN out to $z \sim 3$ (Suh et al. 2017) in the new *Chandra* COSMOS-Legacy survey, which contains 4016 X-ray point sources down to a flux limit of 2.2×10^{-16}, 1.5×10^{-15}, and 8.9×10^{-16} erg cm^{-2} s^{-1} at 20 per cent completeness and in the 0.5–2 keV (soft), 2–10 keV (hard), and 0.5–10 keV (full) bands, respectively (Civano et al. 2016). The optical and IR counterparts, spectroscopic ($z_{\rm spec}$), and photometric ($z_{\rm phot}$) redshifts, and X-ray properties are described in detail in Civano et al. (2016) and Marchesi et al. (2016a). Most of the sources with a $z_{\rm spec}$ have an spectroscopic accuracy >99.5 per cent, while those with a less reliable $z_{\rm spec}$ (spectroscopic accuracy <99.5 per cent) still have $\Delta z = \frac{|z_{\rm spec} - z_{\rm phot}|}{1+z_{\rm spec}} < 0.1$ (see Marchesi et al. 2016a). For these sources, we take the spectroscopic redshift as in Marchesi et al. (2016a). The $z_{\rm phot}$ have been obtained from the spectral energy distribution (SED) of the sources following the procedure described in Salvato et al. (2011): the COSMOS field has been observed in 31 different bands, so the analysis of the SED is equivalent to low-resolution spectroscopy with an accuracy of $\sigma_{(\Delta z/(1+z_{\rm spec}))} = 0.03$. This method produces a nominal value of the $z_{\rm phot}$, corresponding to the maximum of the redshift probability distribution function (PDF). The galaxy properties [mass, age, star formation rate (SFR), and galaxy type] are derived by performing a multiwavelength analysis of the SEDs from far-IR (500μm), when available, to near-UV (ultraviolet; 2300 Å) and using Bayesian statistics. The full details of the SED fitting can be found in Suh et al. (2017). In short, the host galaxy properties are derived via three-component SED fitting decomposition using a nuclear dust torus model (Silva, Maiolino & Granato 2004), a galaxy model (Bruzual & Charlot 2003), and starburst templates (Chary & Elbaz 2001; Dale & Helou 2002). The galaxy model templates are generated using a Chabrier initial mass function and exponentially decaying star formation histories with characteristic times ranging from $\tau = 0.1$ to 30 Gyr and constant star formation. A PDF for galaxy parameters such as stellar mass and SFR is then built to estimate the most representative value for each parameter. The SFR is estimated by combining the contributions from UV and total IR luminosity ($L_{8-1000\,\mu{\rm m}}$). In all cases, the galaxy light dominates the optical emission while the AGN emission peaks at the mid-IR when available. The mid-IR emission of

these dwarf galaxies is however often contaminated by star formation; therefore, the SED of the dwarf galaxies is not dominated by the AGN.

Combining optical spectroscopic and photometric diagnostics, Marchesi et al. (2016a) classify sources into type 1 or unobscured AGN and type 2 and/or obscured AGN (see Marchesi et al. 2016a for details on the classification). Of the type 2 and/or obscured AGN sample, Suh et al. (2017) measured a stellar mass for 2267 sources. From this last sample, we select dwarf galaxies as having the peak of the stellar mass PDF $10^7 \leq M_* \leq 3 \times 10^9$ $M_\odot$. We obtain as a result 51 dwarf galaxies with type 2 AGN, 45 per cent of which (23 sources) have spectroscopic redshifts. Twenty-four out of the 28 sources with photometric redshifts have narrow PDFs and therefore small uncertainties on z, with average 1σ error $\langle \Delta z \rangle \sim 0.02$. The remaining four sources have wide PDFs and/or two peaks in the PDF, and the $z_{\rm phot}$ are therefore poorly constrained, with 1σ errors $\Delta z > 1$. For this reason, we decide not to take into account these four objects in our analysis. This reduces the sample to 47 dwarf galaxies. The average 1σ errors on the stellar mass and SFR derived from the PDF are $\langle \Delta \log M_* \rangle \sim 0.4$ $M_\odot$ and $\langle \Delta {\rm SFR} \rangle \sim 1$ $M_\odot$ yr^{-1}, respectively.

2.1 ULXs in dwarf galaxies

ULXs are typically associated with star-forming galaxies (as inferred from the X-ray luminosity function, e.g. Swartz et al. 2011; Mineo, Gilfanov & Sunyaev 2012a) and are observed to form preferentially in low-metallicity environments and low-metallicity galaxies (e.g. Mapelli, Colpi & Zampieri 2009; Zampieri & Roberts 2009; Mapelli et al. 2010; Prestwich et al. 2013; Brorby, Kaaret & Prestwich 2014). The occurrence of ULXs in dwarf galaxies, which have typically high SFRs and low metallicities, is thus expected to be higher than in more massive galaxies (e.g. Swartz, Soria & Tennant 2008; Walton et al. 2011).

To investigate the presence of ULXs among the sample of 47 dwarf galaxies we apply the main criterion from Mainieri et al. (2010) for selecting ULXs in the COSMOS field: the distance between the X-ray and optical centroid has to be larger than 1.8 times the *Chandra* positional error of the source. This yields seven sources. We note though that dwarf galaxies can have irregular morphologies and that it can be hard to define their dynamical centre of mass, so that the 'central' BH may be anywhere within the core of the galaxy. To confirm the ULX nature of the seven sources, we thus visually inspect the location of their *Chandra* X-ray position on the optical images of the host galaxies. Six out of the seven X-ray detections are clearly located in the outskirts (i.e. beyond the optical extension) of the host galaxies and not only off the optical centre, which makes the criterion used above a reliable way of identifying ULXs. We thus remove the seven sources from the sample in order to have a sample of AGN in dwarf galaxies as clean as possible. A detailed study of these seven ULXs will be reported in a future work. There are four more sources in Figs 1 and 2 that, visually, seem to be ULXs: cid_1201, cid_1261, lid_1755, and lid_3353. The optical/IR identification procedure is done in three bands (3.6 μm, *K* band, and *i* band) using a likelihood ratio (Marchesi et al. 2016a). Very often this results in an association to a red source much brighter in the *K* band that in the optical. This is the case of cid_1201 and cid_1261, whose counterpart is very faint in the *i* band. For cid_1261, the X-ray/optical position offset is due to the low source statistics in the X-ray band. The X-ray emission of lid_1755 also seems slightly offset with respect to the optical centre. However, the object does not accomplish the main ULX exclusion criterion from Mainieri et al. (2010). In lid_3353, the X-ray centroid is located between two potential X-ray sources. Its *Chandra* exposure is relatively low and the point spread function (PSF) is quite poor (the offset from the centre of the observation is >5 arcmin). Yet, the separation of the optical counterpart from the northern X-ray blob is <1 arcsec. The X-ray/optical match for lid_3353 is therefore also correct. Because of all the above, we do not identify cid_1201, cid_1261, lid_1755, and lid_3353 as ULXs. The final sample of dwarf galaxies with type-2 AGN and which constitutes the focus of this paper contains thus 40 sources.

2.2 X-ray analysis

Of the 40 AGN dwarf galaxies with X-ray emission in the *Chandra* COSMOS-Legacy survey, 28 sources have more than 15 net counts in the 0.5–7 keV band. The X-ray fluxes and luminosities of these 28 galaxies have been obtained from a proper spectral fit with an absorbed power-law model. Sources with more than 30 net counts, which is the minimum number to perform a spectral analysis that is reliable (Lanzuisi et al. 2013; Marchesi et al. 2016b), have been analysed in a separate work (Marchesi et al. 2016b) while the spectra of sources having more than 15 and less than 30 net counts have been analysed specifically for this work. All the fits are performed using the Cstat statistics, which is based on the Cash statistics (Cash 1979) and is usually adopted for low-counts spectral fitting, since in principle it does not require counts binning to work. The fits are first performed fixing the power-law photon index to $\Gamma = 1.9$, i.e. a typical AGN value, and leaving the intrinsic absorption $N_{\rm H}$ free to vary. We then repeat the fit leaving both Γ and $N_{\rm H}$ free to vary, and we check if the fit is significantly improved. We assume that a fit is significantly improved if $C{\rm stat}_{\rm old} - C{\rm stat}_{\rm new} > 2.71$ (see e.g. Tozzi et al. 2006; Brightman et al. 2014), where $C{\rm stat}_{\rm old}$ and $C{\rm stat}_{\rm new}$ are the *C*stat values for the fit without and with the photon index free to vary, respectively. In summary, 19 out of 28 sources have a best fit with fixed $\Gamma = 1.9$, while the remaining 9 objects are best-fitted with a model having Γ free to vary. For one source (cid_563) the addition of an **APEC**[1] model to describe thermal emission produces a significant improvement in the fit. We report the best-fitting properties of the 28 dwarf galaxies with more than 15 net counts in the 0.5–7 keV band in Table 1.

For the remaining 12 sources with less than 15 counts, the X-ray fluxes are taken from the recent *Chandra* COSMOS-Legacy catalogue (Civano et al. 2016) and converted to X-ray luminosities, assuming $\Gamma = 1.4$ (which takes into account the fact that obscuration produces a flattening in the observed spectrum) and Galactic $N_{\rm H} = 2.6 \times 10^{20}$ cm^{-2} (Kalberla et al. 2005). The distribution of the full-band X-ray luminosity versus redshift for the 40 X-ray detected dwarf galaxies is plotted in Fig. 3. The solid line represents the 20 per cent completeness flux limit in the full band. Eight of the 40 AGN dwarf galaxies are not detected in the hard band above a maximum likelihood threshold ${\rm DET}_{\rm ML} = 10.8$ (corresponding to a Poisson probability of $P \simeq 5 \times 10^{-5}$ that a detected source is actually a background fluctuation; Civano et al. 2016). We thus consider the 2–10 keV X-ray luminosities of these sources as upper limits in our analysis.

[1] https://heasarc.gsfc.nasa.gov/xanadu/xspec/manual/node133.html

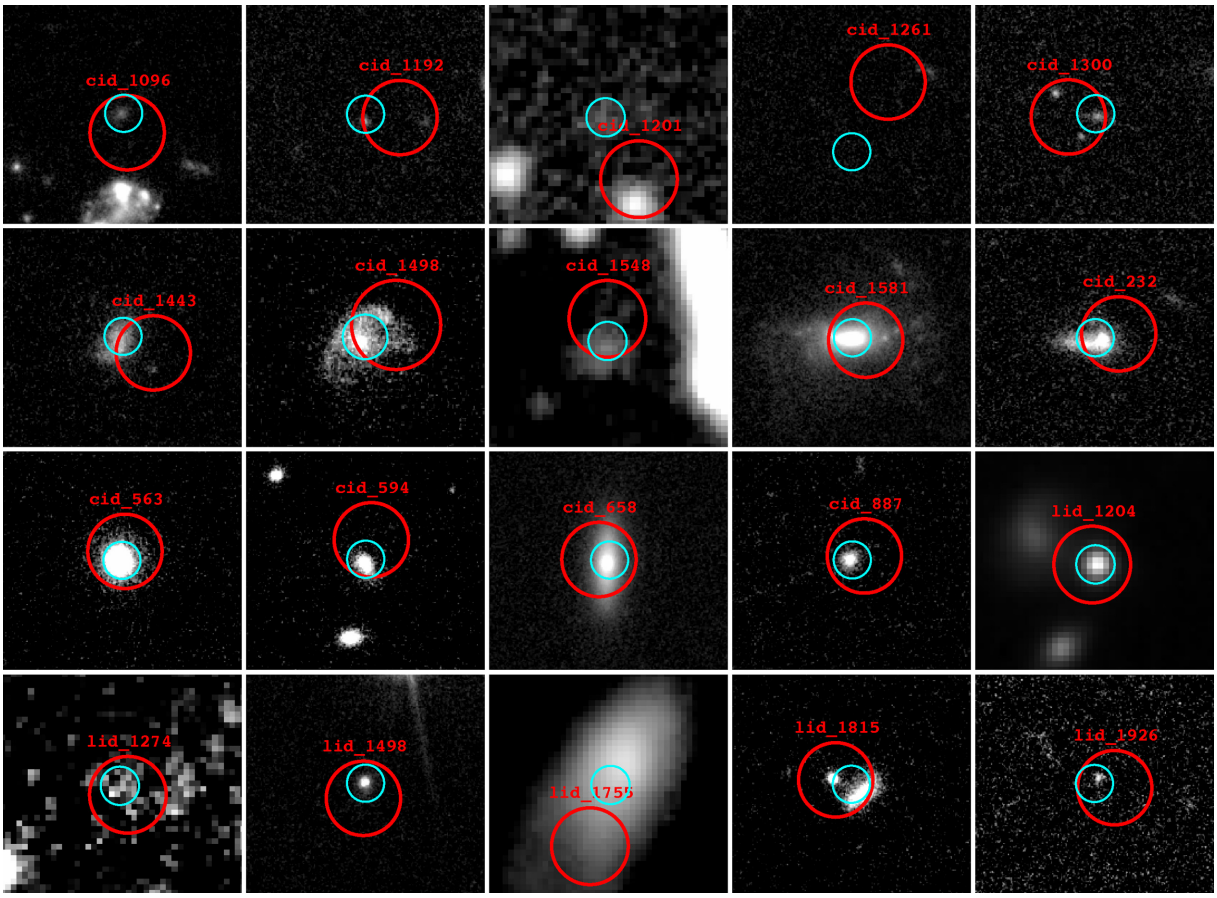

Figure 1. *Hubble Space Telescope* and Subaru *i*-band images of the dwarf galaxies studied in this work. The radius of the red circles denotes a *Chandra* positional error of 1 arcsec. The cyan circles mark the optical position with a positional error of radius 0.5 arcsec.

3 RESULTS AND DISCUSSION

The full-band *K*-corrected 0.5–10 keV X-ray luminosity of the 40 dwarf galaxies ranges from 3.5×10^{39} erg s^{-1} to 9.3×10^{43} erg s^{-1}, with a mean value of $L_{0.5\text{–}10\,\mathrm{keV}} = 1.0 \times 10^{43}$ erg s^{-1} (Fig. 3). Their redshift ranges from 0.03 to 2.39, with mean value of $z = 0.49$ (Fig. 4). This constitutes the highest-z sample of AGN in dwarf galaxies, which were so far limited to the local Universe (e.g. Greene & Ho 2007b, 2007a; Dong et al. 2012; Reines et al. 2013; Schramm et al. 2013) or out to $z < 1$ (Pardo et al. 2016). The range of stellar masses of the 40 dwarf galaxies goes from 6.6×10^7 to 3.1×10^9 M$_\odot$, and the SFR from 2.3×10^{-3} to 46.7 M$_\odot$ yr^{-1} (Table 2), from which we derive specific SFRs (sSFR) in the range of 1.8×10^{-12}–2.6×10^{-8} yr^{-1}. The mean values of the sample are $M_* = 1.4 \times 10^9$ M$_\odot$, SFR = 5.3 M$_\odot$ yr^{-1}, and sSFR = 3.3×10^{-9} yr^{-1}. This classifies most of the galaxies as star forming according to the tight correlation between stellar mass and SFR recognized in the local Universe and intermediate redshifts (e.g. Daddi et al. 2007; Rodighiero et al. 2011). The *Hubble Space Telescope* and Subaru images of the 40 star-forming dwarf galaxies are shown in Figs 1 and 2. The SED fitting provides a morphological classification (Ell-S0, Sa-Sc, Sd-Sdm, starburst) for each dwarf galaxy in our sample. We find that most galaxies (97.5 per cent) qualify as spiral and starburst, in agreement with being star forming as inferred from their sSFR, while only one source is classified as early type. The X-ray luminosity of the 40 dwarf galaxies is more than one order of magnitude higher than the typical X-ray luminosity of X-ray binaries (XRBs), suggesting that the emission is produced by BHs more massive than stellar. However, given the star-forming nature of most of the sources, the observed X-ray luminosity might be a mixed contribution of X-ray emission from XRBs, hot interstellar medium (ISM) gas, and nuclear (AGN) emission. The contribution from XRBs and hot ISM gas must thus be derived and removed from the detected X-ray emission in order to confirm the presence of AGN in the 40 dwarf galaxies. Sections 3.2 and 3.3 describe how this is performed. We will first use the hardness ratio (HR) as a proxy for investigating which type of X-ray emission we are observing.

3.1 Hardness ratio

The X-ray HR is derived as HR = $(H - S)/(H + S)$, where H and S are the count rates in the hard and soft bands, respectively. Obscured AGN ($N_\mathrm{H} > 10^{22}$ cm^{-2}) have typically HR > 0, while unobscured AGN showing unabsorbed soft spectra have HR < -0.1 (e.g. Hasinger 2008; Civano et al. 2012). Thermal emissions from XRBs and hot ISM gas (associated with supernova remnants) have typically HR ≤ -0.8. We show the distribution of HR versus redshift for the sample of 40 dwarf galaxies in Fig. 5, where we also plot the expected HR for thermal emission with $\Gamma = 3$ (dashed

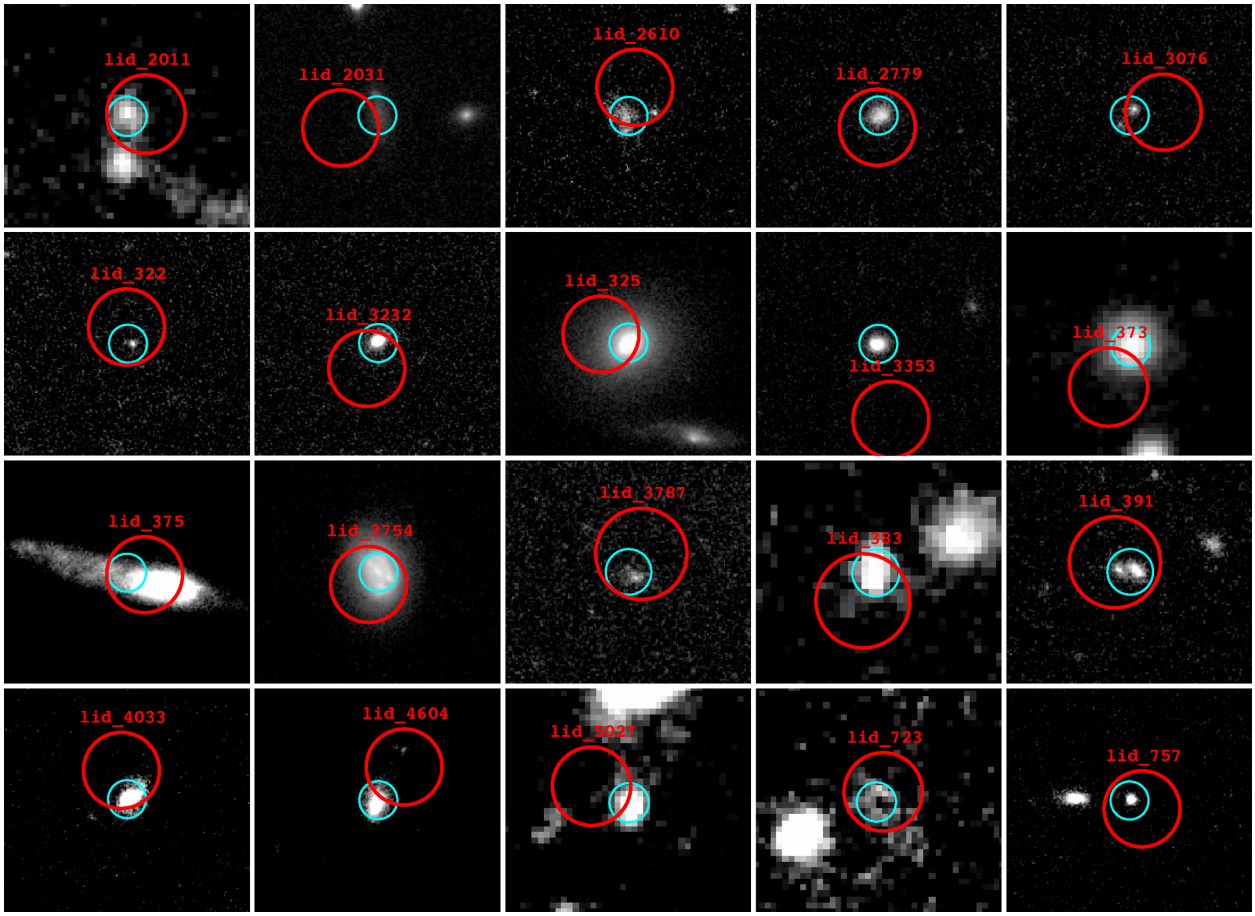

Figure 2. Same caption as in Fig. 1.

line) and for hard X-ray emission (solid lines) from either a population of XRBs or unobscured AGN (tracks at Galactic $N_{\rm H}$ with photon index $\Gamma = 1.4$, $\Gamma = 1.8$, and $\Gamma = 2.2$) and moderately obscured AGN (Galactic $N_{\rm H}$ and $\Gamma = 1$). We find that all the galaxies have an HR above that of thermal emission from e.g. hot ISM gas but consistent with hard X-ray emission, which supports the AGN nature of the X-ray emission of all the galaxies in the sample. To divide the sources into obscured and unobscured AGN, we use HR $= -0.1$. This results in 16 unobscured AGN (with HR < -0.1) and 24 obscured AGN. The fraction of obscured AGN is thus of 60 per cent, consistent with the $\sim 50^{+17}_{-16}$ per cent found by Civano et al. (2016) for the whole *Chandra* COSMOS-Legacy catalogue. The finding that some sources are unobscured despite of their optical classification as type 2 is not unexpected, as a source could be classified as type 2 in the optical not only when the source is obscured but also when the AGN is effectively less luminous than the galaxy light so that the optical SED is dominated by stellar emission (e.g. Civano et al. 2012; Marchesi et al. 2016a).

In order to investigate any redshift evolution of the HR, we derive the mean values for three redshift bins: $0 < z < 0.6$, $0.6 \leq z < 1.0$, and $1.0 \leq z < 2.4$ (Fig. 5). A tendency towards higher HR (i.e. higher column densities) for higher redshifts is observed, indicating a higher level of obscuration as z increases. This is in agreement with an observed increase of the SFR with z, which suggests a higher contribution of XRBs to the X-ray emission for higher redshifts, as was found by Mezcua et al. (2016) for a sample of stacked dwarf galaxies at $z < 1.5$.

3.2 Contribution from XRBs

The contribution from XRBs will come predominantly from young, high-mass X-ray binaries (HMXBs), as low-mass X-ray binaries (LMXBs) typically populate early-type galaxies with very low SFRs and ages above a few Gyr (e.g. see review by Fabbiano 2006). Since a small fraction of the dwarf galaxies (1 source) is of early type, we consider both the contribution from HMXBs and LMXBs to the X-ray emission of the dwarf galaxies. Our sample spans a range of different redshifts and the XRB luminosity evolves with redshift due to a metallicity evolution, with lower metallicity at higher redshift; hence, to estimate the contribution from HMXBs and LMXBs, we use the evolution of their X-ray emission with metallicity (Z) and stellar age (T) derived by Fragos et al. (2013) from population synthesis simulations:

$$\log(L_{\rm X}^{\rm HMXBs}/{\rm SFR}) = \beta_0 + \beta_1 Z + \beta_2 Z^2 + \beta_3 Z^3 + \beta_4 Z^4 \quad (1)$$

erg s^{-1} M$_\odot$ yr, where $0 \leq Z \leq 0.025$ and in the 2–10 keV band $\beta_0 = 40.28 \pm 0.02$, $\beta_1 = -62.12 \pm 1.32$, $\beta_2 = 569.44 \pm 13.71$, $\beta_3 = -1833.80 \pm 52.14$, and $\beta_4 = 1968.33 \pm 66.27$.

$$\log(L_{\rm X}^{\rm LMXBs}/M_*) = \gamma_0 + \gamma_1 \log(T/{\rm Gyr}) + \gamma_2 \log(T/{\rm Gyr})^2 + \gamma_3 \log(T/{\rm Gyr})^3 + \gamma_4 \log(T/{\rm Gyr})^4 \ {\rm erg\ s^{-1}} 10^{10}\ {\rm M_\odot}, \quad (2)$$

where $0 \leq T \leq 13.7$ Gyr and in the 2–10 keV band $\gamma_0 = 40.276 \pm 0.014$, $\gamma_1 = -1.503 \pm 0.016$, $\gamma_2 = -0.423 \pm 0.025$, $\gamma_3 = 0.425 \pm 0.009$, and $\gamma_4 = 0.136 \pm 0.009$.

The 1σ errors on the stellar mass and SFR derived from the PDF are also included in the computation of the $L_{2-10\,{\rm keV}}^{\rm HMXBs}$ and

Table 1. X-ray spectral fitting properties for the 28 dwarf galaxies with more than 15 net counts in the 0.5–7 keV band.

ID	z	cts	SNR	t_{exp} (ks)	*C*stat/d.o.f.	N_H (10^{22} cm^{-2})	Γ	Flux (2–10 keV) (erg s^{-1} cm^{-2})
cid_232	0.165	81.98	9.26	163.20	18.15/25	<0.27	$1.36^{+0.39}_{-0.26}$	8.09×10^{-15}
cid_563*	0.220	84.43	9.13	154.29	26.8/25	<0.09	$1.75^{+0.57}_{-0.38}$	5.44×10^{-15}
cid_594	0.237	118.95	10.37	190.15	37.39/44	$0.30^{+0.29}_{-0.24}$	$1.50^{+0.30}_{-0.28}$	1.24×10^{-14}
cid_658	0.121	252.45	13.76	175.94	79.31/75	$0.92^{+0.51}_{-0.41}$	$1.85^{+0.48}_{-0.43}$	2.18×10^{-14}
cid_887	0.210	69.69	6.30	169.66	16.56/27	$1.36^{+0.85}_{-0.71}$	$2.11^{+0.67}_{-0.60}$	6.02×10^{-15}
cid_1096	0.263	20.24	2.36	196.62	30.85/20	$0.85^{+0.61}_{-0.47}$	1.9	2.30×10^{-15}
cid_1192	2.385	22.95	3.28	160.81	23.32/13	<4.57	1.9	1.28×10^{-15}
cid_1261	1.750	25.24	4.21	127.33	27.0/24	$10.04^{+8.48}_{-5.50}$	1.9	3.90×10^{-15}
cid_1300	0.743	17.88	3.29	176.70	9.71/11	$8.31^{+6.80}_{-3.98}$	1.9	2.73×10^{-15}
cid_1443	0.083	17.88	3.23	168.11	26.12/12	<0.59	1.9	1.04×10^{-15}
cid_1498	0.354	24.95	4.20	159.85	14.74/16	<1.19	1.9	1.21×10^{-15}
cid_1548	0.222	25.88	3.84	183.65	36.57/25	$23.09^{+8.19}_{-6.90}$	1.9	1.38×10^{-14}
cid_1581	0.196	43.85	7.20	172.06	5.14/16	<0.11	1.9	2.78×10^{-15}
lid_322	0.215	73.39	10.23	154.11	37.78/26	$2.85^{+1.28}_{-1.14}$	$2.65^{+0.74}_{-0.67}$	8.43×10^{-15}
lid_373	1.130	20.49	6.12	47.79	14.1/8	<4.81	1.9	3.85×10^{-15}
lid_375	0.08	21.61	3.54	184.79	11.86/23	$0.83^{+0.60}_{-0.49}$	1.9	2.35×10^{-15}
lid_383	0.568	21.35	5.12	78.51	16.53/15	<0.80	1.9	2.44×10^{-15}
lid_391	0.505	148.92	13.18	174.37	45.54/43	$1.51^{+0.63}_{-0.56}$	$1.73^{+0.30}_{-0.28}$	1.51×10^{-14}
lid_723	1.280	52.63	8.89	169.56	20.05/17	<3.87	$0.96^{+0.47}_{-0.40}$	9.26×10^{-15}
lid_757	0.367	135.77	12.46	125.22	46.13/40	<0.09	$1.43^{+0.16}_{-0.15}$	1.65×10^{-14}
lid_1204	0.297	111.73	10.43	77.45	32.12/31	<0.40	$1.30^{+0.31}_{-0.21}$	2.44×10^{-14}
lid_1274	0.976	16.23	3.48	159.76	16.57/10	$11.80^{+6.97}_{-4.49}$	1.9	3.65×10^{-15}
lid_1498	0.186	49.92	8.01	179.54	11.2/15	<0.33	1.9	2.91×10^{-15}
lid_1755	0.054	42.51	7.13	44.57	7.16/12	$0.93^{+0.38}_{-0.32}$	1.9	1.52×10^{-14}
lid_1815	0.273	41.82	5.38	127.69	17.16/17	$0.62^{+0.42}_{-0.35}$	1.9	3.97×10^{-15}
lid_1926	1.282	21.05	3.87	161.80	9.03/11	$3.93^{+2.55}_{-2.05}$	1.9	2.29×10^{-15}
lid_3353	0.278	16.06	3.52	107.81	5.55/14	$1.30^{+1.38}_{-1.05}$	1.9	4.19×10^{-15}
lid_3787	0.085	32.62	5.17	178.30	7.55/10	$5.15^{+2.65}_{-1.72}$	1.9	4.65×10^{-15}

Note. ID is the COSMOS-Legacy X-ray ID; cts are the 0.5–7 keV net counts; SNR is the signal-to-noise ratio in the 0.5–7 keV band; t_{exp} is the exposure time in the 0.5–7 keV band per source; *C*stat/d.o.f. is the *C*stat statistics best-fitting value on the number of degrees of freedom; N_H is the intrinsic absorption; Γ is the photon index; and the 2–10 keV flux is that computed from the X-ray spectrum. *For cid_563, the spectral fit includes an **APEC** model with $kT = 0.54^{+0.43}_{-0.4}$.

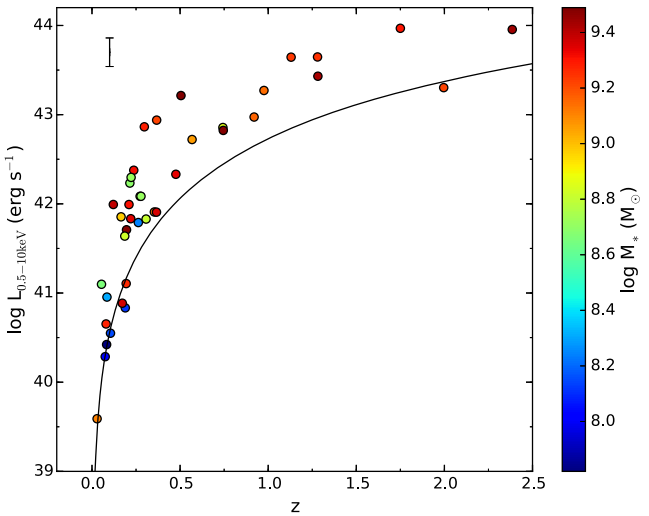

Figure 3. Luminosity (0.5–10 keV) versus redshift for the sample of 40 dwarf galaxies hosting an AGN. The 20 per cent completeness flux limit in the full band is shown with a black solid line. The stellar mass is shown as a colour bar.

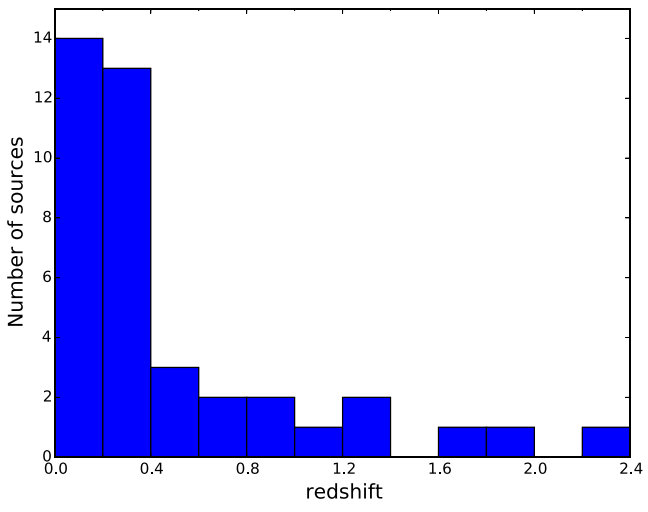

Figure 4. Redshift distribution for the sample of 40 dwarf galaxies. There are 12 sources (30 per cent) with redshifts above 0.5.

$L^{LMXBs}_{2-10\,keV}$. To derive and subtract the XRB contribution ($L^{XRB}_{2-10\,keV}$ $=L^{HMXBs}_{2-10\,keV}+L^{LMXBs}_{2-10\,keV}$) to the detected 0.5–10 keV luminosity of the 40 dwarf galaxies, the $L^{XRB}_{2-10\,keV}$ is converted to the 0.5–10 keV band assuming $\Gamma = 1.4$ (which is a good model for XRB emission; see

Table 2. Host galaxy properties. The average 1σ errors on M_* and SFR are $\sim$0.4 $M_\odot$ and $\sim$1 $M_\odot$ yr^{-1}, respectively.

ID	RA (J2000) (deg)	Dec. (J2000) (deg)	z	log M_* ($M_\odot$)	i (mag)	log SFR ($M_\odot$ yr^{-1})	log $L_{\rm hot}$ (erg s^{-1})	log $L_{\rm XRBs}$ (erg s^{-1})	log $L_{\rm AGN}$ (0.5–10 keV) (erg s^{-1})
(1)	(2)	(3)	(4)	(5)	(6)	(7)	(8)	(9)	(10)
cid_1096	150.115 620	1.951 608	$0.26^{+0.01}_{-0.01}$p	8.24	23.41	− 0.78	38.24 ± 0.01	38.78 ± 0.02	41.8 ± 0.0
cid_1192	149.885 210	2.372 808	$2.38^{+0.37}_{-0.22}$p	9.44	24.81	1.20	40.6 ± 0.2	40.5 ± 0.2	43.9 ± 0.0
cid_1201	149.869 540	2.357 775	$2.00^{+0.95}_{-0.85}$p	9.22	25.93	1.06	40.5 ± 0.2	40.5 ± 0.2	43.3 ± 0.2
cid_1261	150.466 510	2.298 900	$1.75^{+0.53}_{-0.39}$p	9.30	25.43	1.08	40.4 ± 0.2	40.6 ± 0.2	43.9 ± 0.0
cid_1300	150.101 950	2.163 916	$0.74^{+0.11}_{-0.03}$p	8.85	23.90	0.25	39.41 ± 0.08	39.66 ± 0.08	42.9 ± 0.0
cid_1443	150.009 250	2.390 140	0.083 ± 0.000$^{\rm s}$	7.82	22.25	− 1.96	37.00 ± 0.04	37.76 ± 0.05	40.4 ± 0.0
cid_1498	149.773 580	2.141 633	0.354 ± 0.000$^{\rm s}$	9.10	22.28	− 0.36	38.69 ± 0.04	39.15 ± 0.04	41.9 ± 0.0
cid_1548	150.005 845	2.295 230	0.222 ± 0.000$^{\rm s}$	8.72	24.17	0.61	39.62 ± 0.01	40.10 ± 0.02	42.3 ± 0.0
cid_1581	150.628 380	2.414 759	0.196 ± 0.000$^{\rm s}$	9.48	20.15	0.13	39.12 ± 0.05	39.97 ± 0.02	41.7 ± 0.0
cid_232	149.988 640	1.908 585	0.165 ± 0.000$^{\rm s}$	8.97	22.29	− 0.23	38.76±0.07	40.0 ± 0.1	41.9 ± 0.0
cid_563	149.920 540	2.543 668	0.220 ± 0.000$^{\rm s}$	9.35	21.15	− 0.17	40.98*	39.37 ± 0.01	41.8 ± 0.0
cid_594	150.501 346	2.354 369	0.237 ± 0.000$^{\rm s}$	9.32	23.16	− 0.23	38.78 ± 0.07	39.72 ± 0.07	42.4 ± 0.0
cid_658	150.336 048	2.433 799	0.121 ± 0.000$^{\rm s}$	9.39	20.11	− 0.68	38.29 ± 0.01	39.70 ± 0.01	41.9 ± 0.0
cid_887	150.070 390	2.286 302	0.210 ± 0.000$^{\rm s}$	9.31	23.21	− 0.52	38.48 ± 0.07	39.09 ± 0.06	41.9 ± 0.0
lid_1204	150.130 571	1.505 687	$0.30^{+0.01}_{-0.01}$p	9.28	21.49	1.11	40.14 ± 0.01	40.70 ± 0.02	42.9 ± 0.0
lid_1274	150.058 114	1.653 284	$0.98^{+0.05}_{-0.18}$p	9.14	26.33	1.06	40.28 ± 0.03	40.44 ± 0.03	43.3 ± 0.0
lid_1498	150.521 084	1.880 207	$0.19^{+0.01}_{-0.03}$p	8.82	22.89	0.51	39.51 ± 0.05	40.2 ± 0.1	41.61 ± 0.01
lid_1755	150.865 828	2.051 638	$0.05^{+0.02}_{-0.01}$p	8.66	19.92	− 0.36	38.58 ± 0.05	39.36 ± 0.03	41.1 ± 0.0
lid_1815	149.739 201	2.667 379	0.273 ± 0.000$^{\rm s}$	8.83	22.59	− 0.25	38.78 ± 0.08	39.45 ± 0.06	42.1 ± 0.0
lid_1926	150.328 320	2.494 110	$1.28^{+0.16}_{-0.03}$p	9.43	25.35	0.99	40.3 ± 0.1	40.4 ± 0.1	43.4 ± 0.0
lid_2011	150.743 505	2.456 254	0.366 ± 0.000$^{\rm s}$	9.36	24.94	0.42	39.47 ± 0.05	39.93 ± 0.05	41.9 ± 0.2
lid_2031	150.511 100	2.599 287	0.105 ± 0.000$^{\rm s}$	8.15	22.34	− 1.99	36.97 ± 0.05	37.67 ± 0.05	40.6 ± 0.2
lid_2610	149.781 186	1.660 789	$0.74^{+0.03}_{-0.02}$p	9.48	23.73	1.07	40.23 ± 0.02	40.70 ± 0.07	42.8 ± 0.1
lid_2779	150.477 240	1.872 818	$0.19^{+0.02}_{-0.02}$p	8.12	23.32	− 1.05	37.94 ± 0.01	38.50 ± 0.02	40.8 ± 0.2
lid_3076	150.716 114	2.479 516	0.307 ± 0.000$^{\rm s}$	8.81	24.04	− 0.38	38.65 ± 0.09	39.6 ± 0.2	41.8 ± 0.1
lid_322	150.105 140	2.795 295	$0.21^{+0.01}_{-0.02}$p	8.69	24.75	− 1.89	37.11 ± 0.01	38.4 ± 0.2	42.2 ± 0.0
lid_3232	150.717 953	2.788 256	$0.48^{+0.06}_{-0.04}$p	9.34	23.31	− 0.26	38.83 ± 0.04	39.25 ± 0.04	42.3 ± 0.2
lid_325	150.196 073	2.821 245	0.029 ± 0.000$^{\rm s}$	9.11	19.55	− 2.63	36.3 ± 0.02	38.52 ± 0.04	39.5 ± 0.2
lid_3353	149.479 629	2.206 855	0.278 ± 0.000$^{\rm s}$	8.71	22.77	− 0.86	38.16 ± 0.08	39.00 ± 0.07	42.1 ± 0.0
lid_373	149.921 131	2.886 119	$1.13^{+0.03}_{-0.02}$p	9.24	23.23	1.51	40.76 ± 0.05	40.87 ± 0.05	43.6 ± 0.0
lid_375	149.957 674	2.796 841	0.080 ± 0.000$^{\rm s}$	9.27	19.60	− 0.92	38.04 ± 0.02	39.00 ± 0.01	40.6 ± 0.0
lid_3754	150.467 448	1.865 929	0.172 ± 0.000$^{\rm s}$	9.37	20.13	0.22	39.2 ± 0.05	39.97 ± 0.03	40.8 ± 0.3
lid_3787	150.612 276	2.114 749	$0.09^{+0.01}_{-0.01}$p	8.31	22.82	− 0.10	38.86 ± 0.06	39.57 ± 0.06	40.9 ± 0.0
lid_383	150.035 418	2.963 838	$0.6^{+0.2}_{-0.2}$p	9.06	23.77	0.98	40.1 ± 0.02	40.41 ± 0.02	42.7 ± 0.0
lid_391	150.442 403	2.763 864	0.505 ± 0.000$^{\rm s}$	9.49	23.50	1.14	40.24 ± 0.04	40.65 ± 0.04	43.2 ± 0.0
lid_4033	150.408 872	2.509 424	0.194 ± 0.000$^{\rm s}$	9.26	22.98	− 0.52	38.47 ± 0.07	39.17 ± 0.07	41.1 ± 0.2
lid_4604	150.039 578	1.779 599	$0.07^{+0.01}_{-0.01}$p	8.02	21.61	− 1.04	37.91 ± 0.06	39.02 ± 0.09	40.3 ± 0.2
lid_5027	150.777 616	2.420 784	$0.92^{+0.03}_{-0.08}$p	9.16	24.54	0.34	39.54 ± 0.07	40.1 ± 0.2	42.9 ± 0.1
lid_723	149.553 471	2.376 666	$1.28^{+0.34}_{-0.06}$p	9.25	25.34	1.67	40.95 ± 0.01	41.01 ± 0.01	43.6 ± 0.0
lid_757	149.533 635	2.244 504	$0.37^{+0.01}_{-0.02}$p	9.22	23.78	0.29	39.35 ± 0.09	40.3 ± 0.1	42.9 ± 0.0

Note. (1) *Chandra* COSMOS-Legacy X-ray ID, (2) right ascension, (3) declination, (4) redshift, s = spectroscopic, p = photometric, (5) stellar mass, (6) *i*-band magnitude, (7) SFR, (8) 0.5–2 keV X-ray luminosity expected from hot ISM gas estimated using the correlation from Mineo et al. (2012b), (9) 2–10 keV X-ray luminosity expected from XRBs estimated using the correlation from Fragos et al. (2013), (10) 0.5–10 keV AGN X-ray luminosity after removing the contribution from XRBs and hot ISM gas. ∗For cid_563, the $L^{\rm hot}_{0.5-2\,{\rm keV}}$ comes from the fit of the X-ray spectrum with a thermal component in addition to the power-law model.

e.g. Hickox & Markevitch 2006), $N_{\rm H} = 2.6 \times 10^{20}$ cm^{-2} (see Section 2.2), and applying the corresponding *K*-correction factor. We find that the observed $L_{\rm 0.5-10\,keV}$ is more than $\sim 6\sigma$ larger than expected from the $L_{\rm XRB}$ derived from the correlations with Z and T for all the sources and that the contribution from XRBs to the 0.5–10 keV X-ray luminosity is below $\sim$16 per cent. In the hard band, we find that the $L_{\rm 2-10\,keV}$ is $>11\sigma$ above that expected from XRBs and that less than 9 per cent of the XRB emission contributes to the observed 2–10 keV X-ray emission.

The observed $L_{\rm 2-10\,keV}$ versus the hard X-ray luminosity expected from XRBs according to the evolution of $L_{\rm X}^{\rm HMXBs}/{\rm SFR}$ and $L_{\rm X}^{\rm LMXBs}/M_*$ with Z and T (equations 1and 2) is plotted in Fig. 6. In the figure, we also include the stacked 2–10 keV X-ray luminosities of the sample of non-X-ray detected dwarf galaxies from Mezcua et al. (2016), which fill up the gap space of X-ray luminosities $L_{\rm 2-10\,keV} \sim 10^{39}-10^{40}$ erg s^{-1} where no detections are found because of the flux limit of the *Chandra* COSMOS-Legacy survey.

Another correlation that takes into account the redshift evolution of the XRB emission is that found by Lehmer et al. (2016) for a population of normal galaxies at $z \sim$ 0–7:

$$L^{\rm XRB}_{\rm 2-10\,keV} = \alpha_0(1+z)^{\gamma} M_* + \beta_0(1+z)^{\delta}{\rm SFR} \quad (3)$$

in erg s^{-1}, where log $\alpha_0 = 29.30 \pm 0.28$, log $\beta_0 = 39.40 \pm 0.08$, $\gamma = 2.19 \pm 0.99$, $\delta = 1.02 \pm 0.22$, the stellar mass term is pro-

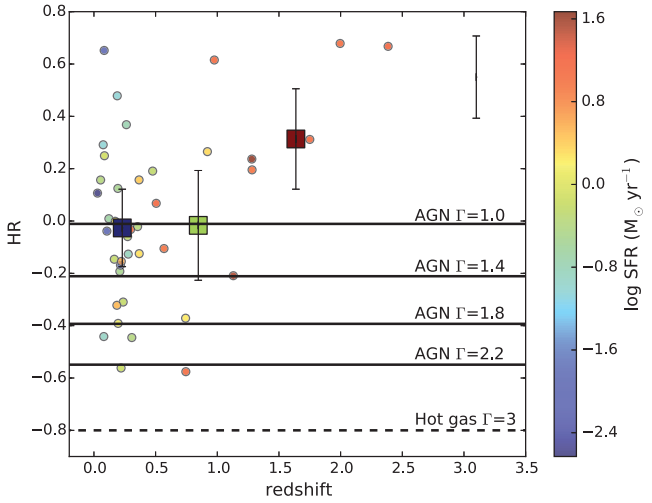

Figure 5. HR versus redshift and SFR (colour bar) for the 40 dwarf galaxies (filled dots). The dashed line indicates the HR of thermal emission with $\Gamma = 3$, the solid lines represent the HR of hard X-ray emission from moderately obscured AGN with photon index $\Gamma = 1$ and Galactic $N_{\rm H} = 2.6 \times 10^{20}$ cm^{-2}, and unobscured AGN with $\Gamma = 1.4$, $\Gamma = 1.8$ and $\Gamma = 2.2$ and Galactic $N_{\rm H}$. The error bar on the top right corner denotes the mean error of the 40 sources. The big squares are the mean HR of the redshift bins: $0 < z < 0.6$, $0.6 \leq z < 1.0$, and $1.0 \leq z < 2.4$.

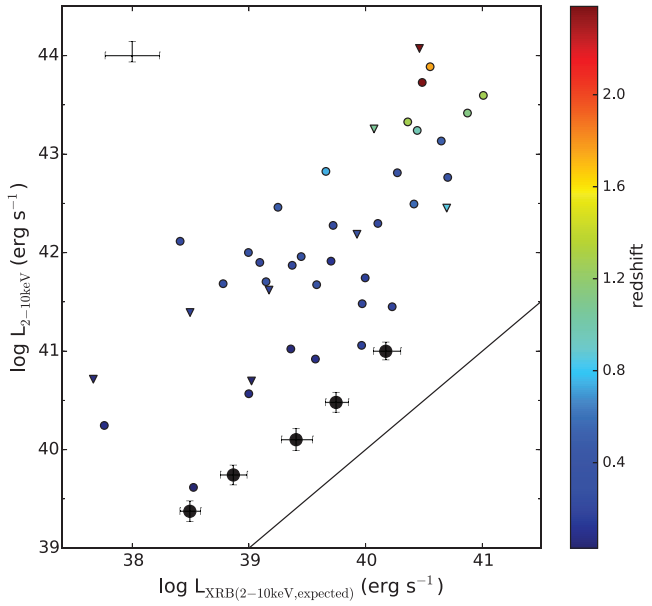

Figure 6. 2–10 keV observed X-ray luminosity of the 40 dwarf galaxies versus expected X-ray luminosity from LMXBs and HMXBs (derived using the evolution of the XRB emission with metallicity and stellar age from Fragos et al. 2013). The grey line shows a one-to-one correlation. The 1σ error bar accounts for the uncertainties on the X-ray fluxes, the SFRs, the M_*, and the errors on the β and γ factors of the Fragos et al. (2013) correlations. Detections in the 2–10 keV are shown as circles and upper limits as inverted triangles. The $L_{2-10\,\rm keV}$ is $>11\sigma$ above the correlation for all the sources. The stacked X-ray luminosities of the sample of X-ray undetected dwarf galaxies from Mezcua et al. (2016) are overplotted as big black dots distributed in five redshift bins ($0 < z \leq 0.3$, $0.3 < z \leq 0.5$, $0.5 < z \leq 0.7$, $0.7 < z \leq 1$, and $1 < z \leq 1.5$).

portional to LMXBs, the SFR term is proportional to HMXBs, and the scatter is of 0.17 dex. We note that those galaxies with $L_{2-10\,\rm keV} < 3 \times 10^{42}$ erg s^{-1} are considered in Lehmer et al. (2016) as star-forming galaxies without an AGN; hence, many of the dwarf galaxies in our sample would be included in the computation of the Lehmer et al. (2016) relation as lacking an AGN. Despite of this, using the Lehmer et al. (2016) relation we find that the observed $L_{0.5-10\,\rm keV}$ is more than $\sim 6\sigma$ larger than expected from the $L_{\rm XRB}$ and that the contribution from XRBs to the 0.5–10 keV X-ray luminosity is below ∼10 per cent.

Using the scaling of $L^{\rm XRB}_{2-10\,\rm keV}$ with M_* and SFR from Lehmer et al. (2010) for luminous star-forming galaxies and no redshift evolution

$$L^{\rm XRB}_{2-10\,\rm keV} = (9.05 \pm 0.37) \times 10^{28} M_* + (1.62 \pm 0.22) \times 10^{39}\ {\rm SFR} \quad (4)$$

and which has a scatter of 0.34 dex, the observed $L_{0.5-10\,\rm keV}$ would be more than $\sim 22\sigma$ larger than expected from the $L_{\rm XRB}-M_*-$SFR correlation for all the sources and the contribution from XRBs to the 0.5–10 keV X-ray luminosity would be below ∼4 per cent. In the hard band, the $L_{2-10\,\rm keV}$ would be more than $\sim 32\sigma$ above that expected from star-forming galaxies and the contribution from XRBs to the 2–10 keV X-ray luminosity would be below ∼3 per cent. Using the $L_{\rm XRB}-M_*-$SFR correlation with no redshift evolution yields thus an X-ray excess significantly higher than that obtained from the Fragos et al. (2013) and Lehmer et al. (2016) relations (e.g. $\gtrsim 22\sigma$ versus $\gtrsim 6\sigma$ in the 0.5–10 keV band). The differences between these correlations and their implication for AGN searches are being explored by Fornasini et al. (in preparation).

There are several caveats that concern the XRB contribution estimate, all of which were investigated in detail in Mezcua et al. (2016). First, we note that the relation between SFR and X-ray luminosity becomes non-linear in the low-SFR regime (Gilfanov, Grimm & Sunyaev 2004), which could decrease the contribution from XRBs for those sources with the lowest SFRs. This issue was explored for the stacked sample of dwarf galaxies (Mezcua et al. 2016), finding that the differences obtained when using a non-linear relation of the form $L_{\rm XRB} \propto {\rm SFR}^{1/(\alpha\,-\,1)}$ were consistent within the errors. Even if significant, the effect of such non-linearity would be to increase the X-ray excess, hence giving further support to the presence of AGN in the sample of dwarf galaxies studied here.

Secondly, the most significant caveat that can affect the XRB contribution estimate is that the metallicity for high redshift and highly star-forming galaxies is expected to be lower than the solar value assumed in the SED fitting (e.g. Lara-López et al. 2010; Yuan, Kewley & Richard 2013; Zahid et al. 2014), which can result in a higher contribution of HMXBs to the integrated X-ray luminosity (e.g. Fragos et al. 2013; Lehmer et al. 2016; Mezcua et al. 2016). To evaluate this effect, we estimate the XRB contribution using the Fragos et al. (2013) correlations, assuming that the metallicity is half solar ($Z = 0.0067$). We find that in this case the $L_{2-10\,\rm keV}$ would still be more than $\sim 7\sigma$ above that expected from XRBs and that the contribution from XRBs to the 2–10 keV X-ray luminosity would be below ∼14 per cent.

3.3 Contribution from hot ISM gas

In star-forming galaxies, the X-ray emission might include some contribution from hot ISM gas in addition to XRBs (e.g. Li & Wang 2013). To estimate the hot ISM contribution to the $L_{0.5-10\,\rm keV}$ of the 40 dwarf galaxies we use the correlation between SFR and diffuse

gas X-ray luminosity ($L^{\rm hot}_{0.5-2\,{\rm keV}}$) from Mineo, Gilfanov & Sunyaev (2012b):

$$L^{\rm hot}_{0.5-2\,{\rm keV}} = (8.3 \pm 0.1) \times 10^{38}\ {\rm SFR}\ ({\rm M}_{\odot}{\rm yr}^{-1}), \quad (5)$$

which has a scatter of 0.34 dex. We convert the $L^{\rm hot}_{0.5-2\,{\rm keV}}$ to the 0.5–10 keV band assuming a power-law index of $\Gamma = 3$ (which is a good representation of a thermal model with temperature ∼0.7–1 keV) and apply the corresponding *K*-correction factor. Using equation (5), we find that the $L_{0.5-10\,{\rm keV}}$ is more than $\sim 34\sigma$ above that expected from hot ISM gas for all the sources and that the contribution of hot ISM to the 0.5–10 keV luminosity is below ∼3 per cent. This is reinforced by the finding that the spectral fitting of those sources with more than 15 counts does not improve by the addition of a thermal component to the power-law model (see Section 2.2). Only for one source, cid_563, are we able to estimate the $L^{\rm hot}_{0.5-2\,{\rm keV}}$ directly from the fit of the X-ray spectrum (see Table 1), finding $\log L^{\rm hot}_{0.5-2\,{\rm keV}} = 40.98\,{\rm erg\,s^{-1}}$ with a large uncertainty (of nearly one order of magnitude). Even when considering these uncertainties, the $L^{\rm hot}_{0.5-2\,{\rm keV}}$ of cid_563 derived from the spectral fitting is significantly higher than its $\log L^{\rm hot}_{0.5-2\,{\rm keV}} = 38.75\,{\rm erg\,s^{-1}}$ estimated from the Mineo et al. (2012b) correlation. Taking the $L^{\rm hot}_{0.5-2\,{\rm keV}}$ derived from the spectral fitting, the $L_{0.5-10\,{\rm keV}}$ of cid_563 is $\sim 5\sigma$ above that from the hot ISM gas and the contribution of the hot ISM to the 0.5–10 keV luminosity for cid_563 is ∼22 per cent. This is two orders of magnitude higher than the contribution from the hot ISM gas that is obtained for cid_563 using equation (5). When feasible, spectral fitting rather than the $L_{\rm X,hot}$−SFR correlation should thus be preferably performed to estimate the contribution from hot gas to the X-ray emission. We use the $\log L^{\rm hot}_{0.5-2\,{\rm keV}} = 40.98\,{\rm erg\,s^{-1}}$ obtained from the spectral fitting to remove the contribution from hot gas to the X-ray emission for cid_563 in the next section.

3.4 AGN emission

We derive the AGN Λemission by subtracting the contribution of XRBs and diffuse hot gas emission from the detected 0.5–10 keV band luminosity. Given that these contributions were not very significant ($\lesssim$16 per cent), we find that the AGN luminosities in the 0.5–10 keV band still range from $\sim 3.5 \times 10^{39}$ to $9.3 \times 10^{43}\,{\rm erg\,s^{-1}}$ in the redshift range of $z = 0.03$–2.39. The finding of AGN in dwarf galaxies at such high redshifts constitutes an unprecedented discovery: Mezcua et al. (2016) found that a population of IMBHs exists in low-mass galaxies out to $z < 1.5$, while the so-far redshift record-holder for an AGN in a low-mass galaxy was source ID 31097, with $z = 0.53$ and $L_{0.5-7\,{\rm keV}} = 1.3 \times 10^{42}\,{\rm erg\,s^{-1}}$ (Pardo et al. 2016). Thanks to the wide area and sensitivity of *Chandra* COSMOS Legacy, we find 12 AGN dwarf galaxies with $z > 0.5$ (Fig. 4) and the new record-holder being cid_1192 ($z = 2.39$, $L_{0.5-10\,{\rm keV}} = 9.0 \times 10^{43}\,{\rm erg\,s^{-1}}$).

The variation of $L_{\rm AGN}$ (0.5–10 keV) with M_* and z is shown in Fig. 7, where we also plot the stacked nuclear X-ray luminosity for five redshift bins out to $z < 1.5$ from Mezcua et al. (2016). The new 40 detected AGN fill the region with $L_{\rm X} > 10^{40}\,{\rm erg\,s^{-1}}$ for $\log M_* < 9.5$, where similar bright ($L_{\rm X} > 10^{40}\,{\rm erg\,s^{-1}}$) AGN dwarf galaxies (e.g. from Reines et al. 2011; Schramm et al. 2013; Reines et al. 2014; Baldassare et al. 2015, 2017; Secrest et al. 2015; Pardo et al. 2016) would be also located. As reported by Mezcua et al. (2016), the lack of high stellar mass sources with low X-ray luminosities observed in Fig. 7 is due to the mass limit of the COSMOS optical/IR survey, while the observed increase of $L_{\rm AGN}$ with stellar mass and redshift is due to the X-ray survey limit. The increase of $L_{\rm AGN}$ with M_* and z could also be caused by the higher SFR found at higher z, which hinders the measure of the AGN contribution, while at lower z (and lower SFR) the AGN contribution can be more easily measured and is thus more significant (Mezcua et al. 2016).

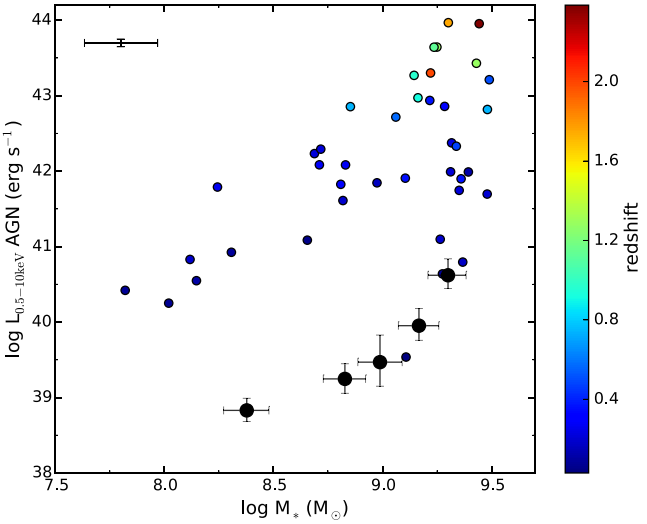

Figure 7. Nuclear X-ray luminosity in the 0.5–10 keV band versus stellar mass for the 40 dwarf galaxies. The error bar on the top left corner denotes the mean error on $L_{\rm AGN}$ and M_* of the sources. The stacked X-ray luminosities of the sample of X-ray undetected dwarf galaxies from Mezcua et al. (2016) are overplotted as big black dots distributed in five redshift bins ($0 < z \leq 0.3$, $0.3 < z \leq 0.5$, $0.5 < z \leq 0.7$, $0.7 < z \leq 1$, and $1 < z \leq 1.5$).

3.5 BH mass and accretion rate

To get an estimate of the BH mass of the 40 dwarf galaxies hosting AGN, we consider the correlation between BH mass and stellar mass found for local AGN (including dwarf galaxies) by Reines & Volonteri (2015): $\log (M_{\rm BH}/{\rm M}_{\odot}) = 7.45 \pm 0.08 + (1.05 \pm 0.11)$ $\log (M_*/10^{11}\ {\rm M}_{\odot})$, with a scatter of 0.55 dex. We find BH masses in the range $M_{\rm BH} = 1.3 \times 10^4 - 7.3 \times 10^5\ {\rm M}_{\odot}$ with a mean value of $M_{\rm BH} = 3.3 \times 10^5\ {\rm M}_{\odot}$, indicating that all the sources are consistent with being IMBHs (see Fig. 8). We note that, although the correlation includes a sample of dwarf galaxies, scaling relations are in general not well calibrated in the low-mass regime (e.g. Martín-Navarro & Mezcua 2018) and thus their use for estimating BH masses in dwarf galaxies is not highly reliable. To quantify such unreliability and be as conservative as possible, we compute the uncertainty on the BH mass considering both the minimum and maximum $M_{\rm BH}$ provided by the 0.55 dex scatter and the minimum and maximum stellar mass derived from the PDF. As a result we find that, when considering these maximized uncertainties on the BH mass, 30 out of 40 of the AGN dwarf galaxies could be as well SMBHs.

To estimate the accretion rate, we derive the Eddington ratio $l_{\rm Edd} = L_{\rm bol}/L_{\rm Edd}$, where $L_{\rm bol}$ is the bolometric luminosity derived from the SED fitting (Suh et al. 2017) and $L_{\rm Edd} = 1.3 \times 10^{38} \times M_{\rm BH}/{\rm M}_{\odot}\,{\rm erg\,s^{-1}}$. The uncertainty on the Eddington ratio estimates is maximized by propagating the uncertainties obtained for the BH mass. The distribution of Eddington ratios is shown as a colour bar in Fig. 8. We find that the Eddington ratio ranges from 7.5×10^{-4} to 1.4×10^2, with a median value of $l_{\rm Edd} = 0.6$. Albeit the large uncertainties, we find that most of the sources (95 per cent) have near- to super-Eddington accretion rates

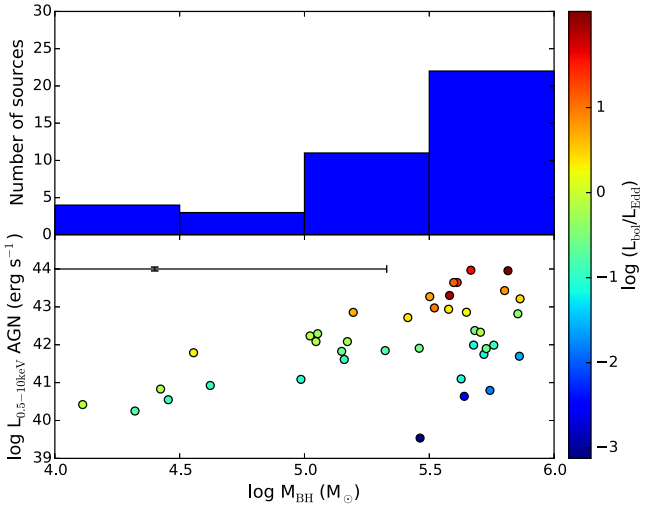

Figure 8. Top: Distribution of BH masses for the 40 dwarf galaxies. The M_{BH} have been estimated using the correlation from Reines & Volonteri (2015). Bottom: AGN luminosity in the 0.5–10 keV band versus BH mass. The error bar on the top left shows the mean error of the L_{AGN} and BH mass. All the sources have $M_{BH} < 10^6$ M$_\odot$ and are thus consistent with being IMBHs. Given the error on the BH mass, those sources with log $M_{BH} \geq 5$ M$_\odot$ cannot be discarded as possible SMBHs. The colour bar denotes the Eddington ratio.

($l_{Edd} > 10^{-2}$), as commonly found in optically selected samples of low-mass BHs in the local Universe for which the BH mass has been derived in more robust ways (e.g. Greene & Ho 2004, 2007b; Dong et al. 2012; Reines et al. 2013; Yuan et al. 2014; Baldassare et al. 2015, 2017). Only two of the AGN dwarf galaxies are found to be accreting at sub-Eddington rates. The high Eddington rates could be explained if BH accretion occurs through short accretion episodes that can reach or even exceed the Eddington limit, as expected from models of early BH growth (e.g. Volonteri & Rees 2005; Madau, Haardt & Dotti 2014; Smole, Micic & Martinović 2015; Pezzulli, Valiante & Schneider 2016; Anglés-Alcázar et al. 2017).

Of particular interest is the finding of a subset of four dwarf galaxies hosting AGN with $M_{BH} = (1.3-2.9)\times 10^4$ M$_\odot$ (Fig. 8). They are at $z < 0.2$, their stellar masses range from $M_* = 6.6 \times 10^7$ M$_\odot$ to 1.4×10^8 M$_\odot$ and they are all near- to super-Eddington accreting ($l_{Edd} = 0.8-1.0$). These sources have the lowest BH mass of the sample and, if the scaling relations hold in this mass regime (though see e.g. Martín-Navarro & Mezcua 2018), they would be the lightest IMBHs ever found in dwarf galaxies (the lightest AGN so far reported are that of the dwarf galaxy RGG 118, with $M_{BH} \sim 5 \times 10^4$ M$_\odot$, Baldassare et al. 2015; and J122732.18+075747.7, with $M_{BH} \sim 4 \times 10^4$ M$_\odot$, Chilingarian et al. 2018). One of them, with $M_* = 6.6 \times 10^7$ M$_\odot$, represents as well the least massive galaxy so far known to host an AGN. A detailed study of these extraordinary IMBHs will be explored in a future work.

3.6 Radio emission

To investigate the presence of radio emission in the sample of dwarf galaxies, we make use of the VLA-COSMOS 3 GHz Large Project source catalogue (Smolcic et al. 2017), which consists of 384 h of deep Karl G. Jansky VLA observations, covering the entire 2 deg^2 COSMOS field at 10 cm (3 GHz) down to an rms of 2.3 μJy beam^{-1} and with a resolution of 0.75 arcsec. We find that 3 out of the 40 dwarf galaxies have a radio counterpart above the VLA-COSMOS threshold of 5.5σ within a radius <1 arcsec from the *Chandra* X-ray counterpart. The redshift of these three sources ranges from $z = 0.03$ to 0.2 and their Eddington ratios from $l_{Edd} = 7 \times 10^{-4}$ to $l_{Edd} = 0.8$ (see Table 3). We convert the 3 GHz radio fluxes to 1.4 GHz, assuming a radio spectral index $\alpha = 0.8$ (typical of star-forming galaxies, Condon 1992; where $S \propto \nu^{-\alpha}$), and find that the *K*-corrected 1.4 GHz radio luminosities of two of the sources are above 10^{24} W Hz^{-1} and thus consistent with an AGN origin (above $L_{1.4\,GHz} = 10^{24}$ W Hz^{-1} the radio emission cannot be explained even by extreme star formation; e.g. Condon 1992; Hickox et al. 2009; Murphy et al. 2011; Goulding et al. 2012; see also Karouzos et al. 2014).

To confirm the AGN origin of the radio emission, we estimate the contribution of star formation to the radio emission using the correlation between 1.4 GHz radio luminosity and SFR for stars massive enough (>5 M$_\odot$) to form supernovae (Condon 1992):

$$L^{SF}_{1.4GHz}(\mathrm{W\ Hz^{-1}}) = 4 \times 10^{21}\ \mathrm{SFR\ (M_\odot\ yr^{-1})}. \quad (6)$$

We find that the fraction of star formation that contributes to the $L_{1.4GHz}$ of the three dwarf galaxies is not significant (≤0.02 per cent) and thus that all the radio emission must come from the AGN. The 1.4 GHz AGN luminosities for the three radio detected dwarf galaxies ranges from 8.49×10^{38} to 6.95×10^{40} erg s^{-1}.

AGN accreting a low Eddington ratios are typically found to be radio-loud (e.g. Ho 2005; Mezcua & Prieto 2014), while (low-mass) AGN with high accretion rates tend to be radio-quiet (e.g. Greene, Ho & Ulvestad 2006), in analogy with XRBs transitioning from a low/hard X-ray state in which a radio jet is present to a high/soft X-ray state in which the jet is quenched (e.g. Remillard & McClintock 2006). The low fraction of radio detections among the sample of 40 AGN dwarf galaxies is thus not unexpected, given that most sources (95 per cent) are accreting at high Eddington rates, but is in agreement with the results of the scarce previous studies of jet radio emission in AGN low-mass galaxies: e.g. Greene et al. (2006) find only one radio-loud AGN out of a sample of 19 low-mass active galaxies, and only four other AGN dwarf galaxies have been reported to have a radio jet (NGC 4395, Wrobel & Ho 2006; NGC 404, Nyland et al. 2012; Mrk 709, Reines et al. 2014; Henize 2–10, Reines et al. 2011, Reines & Deller 2012, though the presence of an AGN in this dwarf galaxy is controversial, Cresci et al. 2017). The presence of collimated radio emission is yet also possible in BHs with high accretion rates (e.g. Pakull, Soria & Motch 2010; Soria et al. 2014; Kaaret, Feng & Roberts 2017), which could be the case of lid_322. The large uncertainties on the Eddington ratio could also explain the high accretion rate of this source.

The detection of jet radio emission spatially coincident with hard X-ray emission has been often used to estimate the BH mass by means of the Fundamental Plane of accreting BHs (e.g. Reines et al. 2011, 2014; Mezcua & Lobanov 2011; Hlavacek-Larrondo et al. 2012; Webb et al. 2012; Mezcua et al. 2013a,b, 2015, 2018; Koliopanos et al. 2017), which is a correlation between nuclear X-ray luminosity, core radio luminosity, and BH mass valid from stellar-mass BHs to SMBHs in the hard X-ray spectral state (e.g. Falcke, Körding & Markoff 2004). Several correlations with different scatters exist based on different samples with varied properties: e.g. the correlation from Merloni, Heinz & di Matteo (2003) has the largest scatter (0.88 dex) as it includes both flat and steep radio sources, different accretion rates, and BH masses estimated using different methods; Gültekin et al. (2009) use only dynamical BH masses and nuclear radio sources, which reduces the scatter to 0.77 dex; Plotkin et al. (2012) include only sub-Eddington accreting sources and a Bayesian approach, which yields a scatter of 0.07 dex

Table 3. Radio properties of the three dwarf galaxies detected with the VLA at 3 GHz.

ID	z	Total (μJy)	Peak (μJy beam^{-1})	Resolved	Separation (arcsec)	$L_{\rm AGN}$ (1.4 GHz) (erg s^{-1} cm^{-2})	$L_{\rm bol}/L_{\rm Edd}$
cid_887	0.210	21.7 ± 2.5	21.7	no	0.28	$(7.0 \pm 0.8) \times 10^{40}$	7×10^{-2}
lid_322	0.215	18.0 ± 2.5	18.0	no	0.35	$(6.1 \pm 0.9) \times 10^{40}$	8×10^{-1}
lid_325	0.029	17.2 ± 2.5	17.2	no	0.91	$(8.5 \pm 1.2) \times 10^{38}$	7×10^{-4}

Note. (1) *Chandra* COSMOS-Legacy X-ray ID, (2) redshift, (3) total flux at 3 GHz, (4) peak flux at 3 GHz, (5) radio emission resolved, (6) separation between the radio and X-ray counterpart, (7) 1.4 GHz AGN radio luminosity derived assuming a radio spectral index $\alpha = 0.8$ and after removing the contribution from star formation, (8) Eddington ratio.

(see e.g. Mezcua et al. 2018 for a brief review). Given the range of accretion rates of the three dwarf galaxies with radio counterparts and their inferred IMBH nature (Section 3.5), we obtain a second estimate of their BH mass using the Fundamental Plane from Gültekin et al. (2009), which is the only one proven to be valid in the IMBH regime (Gültekin et al. 2014):

$$\log L_{\rm R} = (4.80 \pm 0.24) + (0.78 \pm 0.27)\log M_{\rm BH} + (0.67 \pm 0.12)\log L_{\rm X}, \quad (7)$$

where $L_{\rm R}$ and $L_{\rm X}$ are the 5 GHz core radio luminosity and 2–10 keV band nuclear X-ray luminosity, respectively, in erg s^{-1}. We derive $L_{\rm R}$ by taking the peak of 3 GHz radio emission and converting it to 5 GHz assuming $\alpha = 0.8$. For the $L_{\rm X}$, we take the 2–10 keV AGN X-ray luminosities derived in Section 3.4. Given the resolution of the VLA-COSMOS observations, the 5 GHz AGN radio luminosities are most likely a combination of core and lobe radio emission; hence, the BH masses estimated using the Fundamental Plane should be taken as upper limits. We find that the BH masses are $\log M_{\rm BH} < 6.5$ with a scatter of 0.77 dex. Further uncertainties on these mass estimates also arise from the finding of a second track in the Fundamental Plane (Gallo, Miller & Fender 2012) and the lack of a correlation between the BH mass and the radio/X-ray plane for XRBs (Gallo et al. 2014).

3.7 Mid-IR AGN selection

The IR emission of reprocessed light by heated dust produces different mid-IR colours depending on whether AGN, stars or non-active galaxies are the source of the heating. Mid-IR colour–colour diagrams have thus become a widely used tool for identifying AGN based on either the *Spitzer*/IRAC (e.g. Lacy et al. 2004, 2007; Stern et al. 2005) or the *Wide-field Infrared Survey Explorer* (e.g. Stern et al. 2012) bands at 3.6, 4.5, 5.8, and 8.0μm. The mid-IR emission from AGN-heated dust is, in addition, less sensitive to obscuration than in the X-rays; hence, mid-IR selection techniques are able to identify heavily obscured AGN missed even by deep X-ray surveys (e.g. Donley et al. 2008).

Several studies have used mid-IR colour cuts for selecting AGN in dwarf galaxies (e.g. Satyapal et al. 2014; Sartori et al. 2015; Marleau et al. 2017). However, star-forming dwarf galaxies can have mid-IR colours similar to those of luminous AGN (Hainline et al. 2016). Mid-IR colour diagrams are thus not a very reliable tool for selecting AGN in dwarf galaxies. To probe this, we perform a mid-IR colour–colour cut for those AGN dwarf galaxies for which the four IRAC bands are available (20 out of the 40 dwarf galaxies; see Table 4). Nearly half (9 out of 20) of the AGN dwarf galaxies are classified as AGN according to the IRAC criteria of Lacy et al. (2004, 2007). When including the more stringent criteria of Donley et al. (2012), which aims at minimizing contamination from high-redshift star-forming galaxies in deep IRAC surveys, only two of the galaxies qualify as AGN (see Fig. 9). None of the dwarf galaxies qualify as AGN when using the Stern et al. (2005) magnitude colour cut. These results are independent of the level of obscuration, as sources with low HR (i.e. low obscuration) are located both inside and outside the AGN locus (see colour bar in Fig. 9). When the AGN dominates over the galaxy light, IRAC AGN-selection is very powerful in identifying luminous both obscured and unobscured AGNs (i.e. it is able to identify up to 95 per cent of luminous AGNs regardless of obscuration; Hao et al. 2010, 2011). However, it is not effective in identifying low-luminosity AGN with host-dominated mid-IR SEDs nor luminous heavily obscured AGN with bright host galaxies (Donley et al. 2012). The UV/optical-to-IRAC bands are dominated by host galaxy light in our dwarf galaxies, most of which (90 per cent) are low-luminosity AGN[2] with $L_{0.5\text{–}10\,\rm keV} < 3.1 \times 10^{43}$ erg s^{-1} and the rest luminous AGN ($L_{0.5\text{–}10\,\rm keV} \geq 3.1 \times 10^{43}$ erg s^{-1}) with moderate-to-high obscuration (HR > 0; see Fig. 5). This explains the low number of IRAC colour-selected AGN dwarf galaxies, which is in agreement with the results from Donley et al. (2012) in which many X-ray-detected AGNs are outside the Lacy et al. and Stern et al. wedges. The results thus favour the use of X-ray detections as a very good method to find AGN missed by other selection criteria (i.e. mid-IR).

Table 4. IRAC fluxes (in μJy).

ID	F (3.6 μm)	F (4.5 μm)	F (5.8 μm)	F (8.0 μm)
cid_1548	15.1 ± 0.1	18.5 ± 0.1	22.4 ± 3.1	14.8 ± 4.4
cid_232	64.5 ± 0.6	71.6 ± 0.4	73.2 ± 2.2	94.4 ± 2.7
cid_563	17.9 ± 0.2	19.0 ± 0.2	10.1 ± 3.8	59.5 ± 3.4
cid_887	26.1 ± 0.2	22.4 ± 0.1	19.4 ± 4.1	1.2 ± 4.4
lid_1204	57.2 ± 0.3	64.3 ± 0.4	72.9 ± 3.0	83.2 ± 5.4
lid_1274	3.86 ± 0.08	5.8 ± 0.1	5.8 ± 1.6	0.8 ± 1.8
lid_1498	29.1 ± 0.7	32.2 ± 0.5	30.4 ± 1.7	23.7 ± 3.4
lid_1755	92.9 ± 0.3	75.1 ± 0.5	59.2 ± 6.7	198.1 ± 18.1
lid_1815	8.0 ± 0.1	9.4 ± 0.1	22.4 ± 4.7	20.9 ± 3.8
lid_2011	21.7 ± 0.1	23.3 ± 0.1	18.6 ± 5.1	12.1 ± 4.3
lid_2610	8.1 ± 0.1	7.83 ± 0.09	3.2 ± 1.9	8.9 ± 3.9
lid_3076	15.1 ± 0.2	18.7 ± 0.2	16.3 ± 3.1	7.9 ± 3.2
lid_322	12.4 ± 0.1	15.3 ± 0.1	14.8 ± 2.1	11.6 ± 4.2
lid_325	131.6 ± 0.6	93.6 ± 0.7	45.5 ± 5.5	27.8 ± 5.8
lid_375	133.5 ± 0.6	96.3 ± 0.5	76.2 ± 8.3	298.4 ± 14.6
lid_3787	55.1 ± 3.8	55.4 ± 2.9	42.7 ± 10.6	21.2 ± 10.2
lid_391	23.8 ± 0.3	27.9 ± 0.3	33.0 ± 2.7	61.0 ± 5.5
lid_4033	32.0 ± 0.2	26.4 ± 0.2	23.4 ± 4.7	13.0 ± 5.7
lid_4604	21.0 ± 0.2	21.0 ± 0.2	21.1 ± 4.9	3.9 ± 2.9
lid_723	5.93 ± 0.06	6.44 ± 0.07	7.8 ± 1.5	6.2 ± 2.2
lid_757	13.5 ± 0.1	16.3 ± 0.1	15.3 ± 2.1	15.5 ± 3.7

[2]Low-luminosity AGNs are typically defined as having $L_{\rm bol} \leq 10^{42}$ erg s^{-1} (e.g. Ho 2008; Mezcua & Prieto 2014). We consider here the AGN X-ray luminosity instead of the bolometric luminosity just to use the same criterion as Donley et al. (2012), relevant to this discussion.

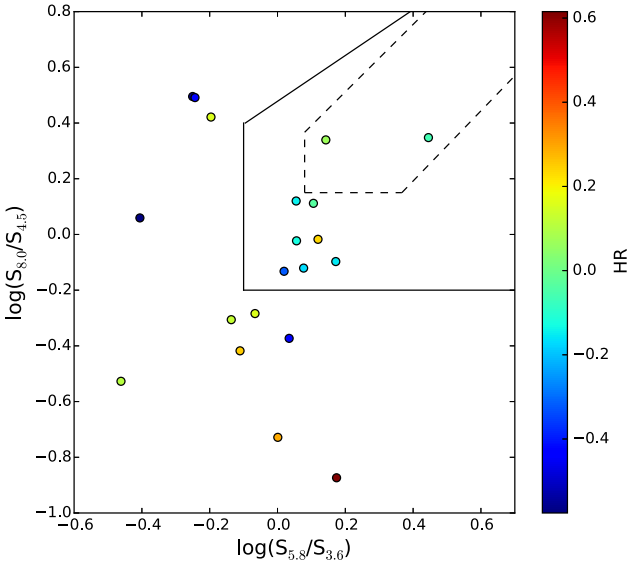

Figure 9. IRAC colour–colour plot for the 20 AGN dwarf galaxies for which IRAC fluxes in the 3.6, 4.5, 5.8, and 8.0 μm bands are available. The solid line delimites the AGN selection region of Lacy et al. (2004, 2007). The dashed wedge is the most stringent AGN selection criteria of Donley et al. (2012), which minimizes contamination from high-redshift star-forming galaxies. The HR is shown as a colour bar.

3.8 AGN fraction in dwarf galaxies

Those dwarf galaxies (52 508 sources) within the area covered by the *Chandra* COSMOS-Legacy survey with no X-ray emission were studied by Mezcua et al. (2016), who divided the sources in five redshift bins out to $z = 1.5$ ($0 < z \leq 0.3$, $0.3 < z \leq 0.5$, $0.5 < z \leq 0.7$, $0.7 < z \leq 1$, and $1 < z \leq 1.5$) complete above the optical limit provided by the *K*-band sensitivity limit of the COSMOS survey (McCracken et al. 2012; Laigle et al. 2016), for which in Mezcua et al. (2016) we took a conservative value of 23.0 mag. By including the 40 AGN dwarf galaxies found here we are able to study, for the first time, the evolution with redshift, stellar mass, and X-ray luminosity of the AGN fraction in dwarf galaxies out to $z = 0.7$, down to $L_{0.5\text{–}10\,\mathrm{keV}} \sim 10^{41}$ erg s^{-1} and down to a stellar mass range $10^7 \leq M_* \leq 1 \times 10^9$ M$_\odot$ (Fig. 10).

We use two X-ray luminosity bins ($3.7 \times 10^{41} \leq L_{0.5\text{–}10\,\mathrm{keV}} < 2.4 \times 10^{42}$ erg s^{-1} and $L_{0.5\text{–}10\,\mathrm{keV}} \geq 2.4 \times 10^{42}$ erg s^{-1}) complete above the 20 per cent flux limit in the 0.5–10 keV band (see Fig. 3). The bins are determined by drawing an horizontal line from the solid curve to the left in Fig. 3, as performed in Mezcua et al. (2016) for the stacking analysis (see fig. 2 in Mezcua et al. 2016), so that for all sources in each bin we are complete at 80 per cent. To investigate any possible loss of sources due to completeness, we also use the prescription of Aird et al. (2012; see their section 5.1 for a detailed description) to compute a conditional probability density function $p(L_X|M_*, z)$ that describes the probability of a galaxy of a given M_* and z to host an AGN with luminosity L_X. As we will see, the results obtained using both methods are consistent.

For the highest $L_{0.5\text{–}10\,\mathrm{keV}}$ bin, we are able to derive the AGN fraction in three complete redshift bins ($0 < z \leq 0.3$, $0.3 < z \leq 0.5$, and $0.5 < z \leq 0.7$; Fig. 10, bottom panel). For the lowest $L_{0.5\text{–}10\,\mathrm{keV}}$ bin, we are able to compute the AGN fraction in two complete stellar mass bins ($10^7 \leq M_* \leq 10^9$ M$_\odot$ and $10^9 < M_* \leq 3 \times 10^9$ M$_\odot$) for $z \leq 0.3$ (Fig. 10, top panel). In each complete redshift/luminosity/stellar mass bin, the AGN fraction is calculated

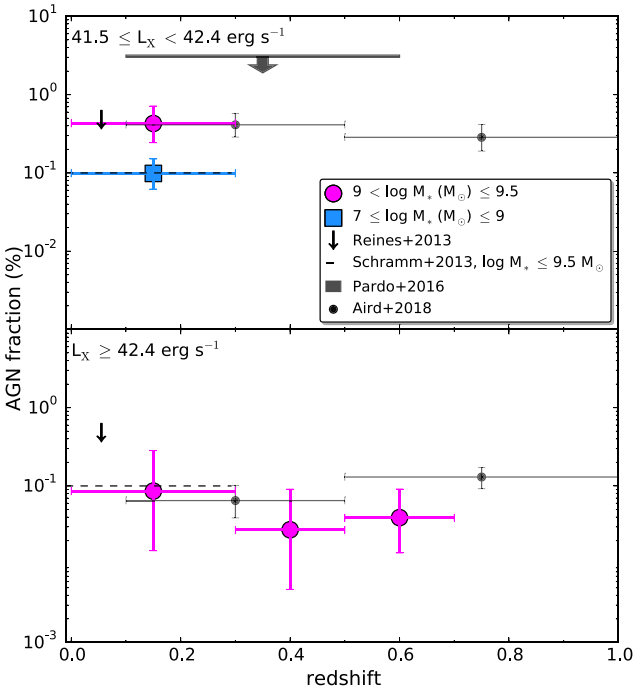

Figure 10. AGN fraction as function of redshift for $3.7 \times 10^{41} \leq L_{0.5\text{–}10\,\mathrm{keV}} < 2.4 \times 10^{42}$ erg s^{-1} (top panel) and $L_{0.5\text{–}10\,\mathrm{keV}} \geq 2.4 \times 10^{42}$ erg s^{-1} (bottom panel). We further bin in stellar mass: $10^7 \leq M_* \leq 10^9$ M$_\odot$ (blue square) and $10^9 < M_* \leq 3 \times 10^9$ M$_\odot$ (magenta circles). We plot for comparison the AGN fraction from Schramm et al. (2013) for $M_* \leq 3 \times 10^9$ M$_\odot$ uncorrected from incompleteness; the upper limit from Reines et al. (2013) for optically selected dwarf galaxies with $10^7 \leq M_* \leq 3 \times 10^9$ M$_\odot$ at $z < 0.055$, the AGN fraction from Pardo et al. (2016) for $10^9 \leq M_* \leq 3 \times 10^9$ M$_\odot$ and $0.1 < z < 0.6$ (shown as an upper limit given their low statistics), and the AGN fraction from Aird et al. (2018) for $9 < \log M_*$ (M$_\odot$) < 9.5.

as $f_{\mathrm{AGN}} = N_{\mathrm{AGN}}/N_{\mathrm{total}}$ where $N_{\mathrm{total}} = (N_{\mathrm{undetected}} + N_{\mathrm{AGN}})$, N_{AGN} is the number of AGN dwarf galaxies and $N_{\mathrm{undetected}}$ the number of dwarf galaxies with no X-ray detections from Mezcua et al. (2016) in each redshift and stellar mass bin. Because of the low number of detections, we use Poisson statistics to compute a lower and upper value of the AGN fraction in each bin complete in X-ray luminosity, redshift, and stellar mass.

We note that by performing an X-ray stacking of the X-ray undetected dwarf galaxies, Mezcua et al. (2016) found an X-ray excess attributed to AGN emission. The AGN fractions derived here represent thus a lower limit on the fraction of active BHs in dwarf galaxies. Furthermore, all the AGNs in the dwarf galaxies studied in this paper are of type 2. The catalogue of X-ray point sources from the *Chandra* COSMOS-Legacy survey (Civano et al. 2016) contains 2716 type-2 AGNs and 985 type-1 AGNs (Marchesi et al. 2016a; Suh et al. 2017; Suh private communication). If the same ratio of type-1/type-2 AGN holds in dwarf galaxies, the addition of the type-1 sources would further increase the AGN fraction in dwarf galaxies.

We find that the AGN fraction for $z \leq 0.3$ is 0.43 per cent for $3.7 \times 10^{41} \leq L_{0.5\text{–}10\,\mathrm{keV}} < 2.4 \times 10^{42}$ erg s^{-1} and $10^9 < M_* \leq 3 \times 10^9$ M$_\odot$ and that it decreases with stellar mass to $f_{\mathrm{AGN}} = 0.1$ per cent for $10^7 \leq M_* \leq 10^9$ M$_\odot$ (see Fig. 10, top panel) and with X-ray luminosity to $f_{\mathrm{AGN}} = 0.09$ per cent for $L_{0.5\text{–}10\,\mathrm{keV}} \geq 2.4 \times 10^{42}$ erg s^{-1} (Fig. 10, top and bottom panels). The conditional probability density function for $z \leq 0.3$ presents the same behaviour: it is

$p = 0.46$ per cent for $3.7 \times 10^{41} \leq L_{0.5\text{–}10\,\mathrm{keV}} < 2.4 \times 10^{42}$ erg s^{-1} and $10^9 < M_* \leq 3 \times 10^9$ M$_\odot$, decreases to $p = 0.11$ per cent for $10^7 \leq M_* \leq 10^9$ M$_\odot$ and to $p = 0.06$ per cent for $L_{0.5\text{–}10\,\mathrm{keV}} \geq 2.4 \times 10^{42}$ erg s^{-1}, which are in agreement with the values of the AGN fractions.

For $z \leq 0.3$, $10^9 < M_* \leq 3 \times 10^9$ M$_\odot$, and $3.7 \times 10^{41} \leq L_{0.5\text{–}10\,\mathrm{keV}} < 2.4 \times 10^{42}$ erg s^{-1}, the upper value of the AGN fraction derived from Poisson statistics ($f_{\mathrm{AGN}} = 0.72$ per cent) is consistent with the AGN fraction range of 0.6–3 per cent found by Pardo et al. (2016) for $L_{\mathrm{X}} \geq 10^{41}$ erg s^{-1} and $0.1 < z < 0.6$ using a sample of dwarf galaxies from the NEWFIRM Medium Band Survey with data in the AEGIS field. We note that the range of values derived by Pardo et al. (2016) are based on very few detections (e.g. on a single detection in the case of their lower limit of 0.6 per cent), and therefore, their AGN fraction should be considered as an upper limit, given the low statistics (Fig. 10, top panel). The $z \leq 0.3$ AGN fraction for $10^9 < M_* \leq 3 \times 10^9$ M$_\odot$ and $3.7 \times 10^{41} \leq L_{0.5\text{–}10\,\mathrm{keV}} < 2.4 \times 10^{42}$ erg s^{-1} is also in agreement with the local AGN fraction found by Reines et al. (2013) (∼0.5 per cent) for a sample of optically selected dwarf galaxies in the same stellar mass range but not corrected for incompleteness (and thus considered as an upper limit). The AGN fraction at $z \leq 0.3$ agrees as well with the value of ∼0.1 per cent derived by Pardo et al. (2016) for the sample of X-ray-detected dwarf galaxies found by Schramm et al. (2013) in the *Chandra* Deep Field-South, albeit of the incompleteness of the Schramm et al. (2013) sample. Miller et al. (2015) find an AGN fraction for local early-type galaxies with $M_* < 10^{10}$ M$_\odot$ of >20 per cent, which is much larger than the values found here. However, the galaxies in Miller et al. (2015) are highly sub-Eddington while most of the AGN dwarf galaxies found here have Eddington ratios $\gtrsim$10 per cent (as those in Reines et al. 2013 and Pardo et al. 2016) and are spiral and starburst.

Shi et al. (2008) study the evolution of AGN fraction with stellar mass, finding that for low-mass galaxies with $10^{9.7} < M_* < 10^{10.3}$ M$_\odot$ and $L_{2\text{–}8\,\mathrm{keV}} > 10^{42}$ erg s^{-1} the AGN fraction is 0.3 per cent for $0.1 < z < 0.4$ (see fig. 7 in their paper). Despite the slightly different stellar mass regime probed in their study, their value is in remarkably excellent agreement with the upper value of the AGN fraction ($f_{\mathrm{AGN}} = 0.28$ per cent) at $z \leq 0.3$ for $L_{0.5\text{–}10\,\mathrm{keV}} \geq 2.4 \times 10^{42}$ erg s^{-1}. Shi et al. (2008) also find that the AGN fraction increases with stellar mass, e.g. from 0.3 per cent for $M_* < 10^{10.3}$ to 1 per cent for $M_* > 10^{10.5}$ M$_\odot$ and $0.1 < z < 0.4$, in agreement with the increase of AGN fraction with stellar mass for galaxies up to 10^{11} M$_\odot$ found by Kauffmann et al. (2003) for $z < 0.3$. Although we probe a much narrower range of stellar masses, such a trend is also observed in Fig. 10 (top panel), in which the AGN fraction for $z \leq 0.3$ increases from 0.1 per cent for $10^7 \leq M_* \leq 10^9$ M to 0.43 per cent for $10^9 < M_* \leq 3 \times 10^9$ M$_\odot$.

Aird et al. (2012) ⊙and Aird, Coil & Georgakakis (2018) have studied in detail the evolution of AGN fraction with redshift, X-ray luminosity, and stellar mass using data from the PRIMUS survey, COSMOS, and the CANDELS fields, probing stellar masses down to $8.5 < \log M_* < 9$ M$_\odot$ and X-ray luminosities down to $L_{2\text{–}10\,\mathrm{keV}} \sim 10^{41}$ erg s^{-1}. The authors find that the AGN fraction decreases with decreasing stellar mass, in agreement with our results and with previous studies, and that for $\log M_* = 9.25$ M$_\odot$ and $\log L_{0.5\text{–}10\,\mathrm{keV}} \sim 41.4$ erg s^{-1} (Aird private communication), the AGN fraction seems to drop with redshift (albeit with large uncertainties, so it could as well be consistent with constant). To compare these results to ours, we plot in Fig. 10 (bottom panel) the AGN fraction found by Aird et al. (2018) for star-forming galaxies with $9 < \log M_*$ (M$_\odot$) < 9.5 at redshift $z \sim 0.3$ and $z \sim 0.7$. At $z \sim 0.3$, their values are fully consistent with ours both for $3.7 \times 10^{41} \leq L_{0.5\text{–}10\,\mathrm{keV}} < 2.4 \times 10^{42}$ erg s^{-1} and $L_{0.5\text{–}10\,\mathrm{keV}} \geq 2.4 \times 10^{42}$ erg s^{-1}.

For $L_{0.5\text{–}10\,\mathrm{keV}} \geq 2.4 \times 10^{42}$ erg s^{-1}, we also find a possible decrease of AGN fraction with redshift, at least out to $z = 0.5$, of the form $f_{\mathrm{AGN}} \propto z^{-0.3 \pm 0.1}$ (correlation coefficient $r^2 = 0.6$). We note though that the values are consistent when considering the uncertainties derived from Poisson statistics. The behaviour of the AGN fraction of dwarf galaxies is, in any case, significantly different than that of more massive galaxies (for which there is a significant increase in AGN fraction from $z \sim 0.1$ to $z \sim 2$; see fig. 6 in Aird et al. 2018), suggesting that the AGN evolution in dwarf galaxies is very different to that of massive galaxies and that BH growth seems to be suppressed in the low-mass regime (Aird et al. 2018).

The low AGN fraction in dwarf galaxies and their possible decrease with redshift (Fig. 10, bottom panel) could be explained if the BH switches on and off on very short time-scales, specially at high redshifts, in agreement with observational constraints (e.g. Schawinski et al. 2015) and models in which BH growth is dominated by short episodes of accretion at high Eddington rates (e.g. Volonteri & Rees 2005; Madau et al. 2014; Smole et al. 2015; Pezzulli et al. 2016; Anglés-Alcázar et al. 2017). This could also explain the low number of detections of the high-z SMBH progenitors, which, even when taking obscuration into account, should be bright enough to be detected by current wide-area X-ray surveys such as *Chandra* COSMOS Legacy (Pezzulli et al. 2017b).

Numerical simulations also predict that the early growth of BHs in low-mass galaxies is significantly suppressed by bursty stellar feedback, which continuously evacuates gas from the nucleus, so that efficient BH growth begins when the stars dominate the gravitational potential in the nucleus and star formation becomes less bursty, which roughly corresponds to galaxies growing to $M_* > 10^{9.5}$ M$_\odot$ (e.g. Dubois et al. 2015; Anglés-Alcázar et al. 2017; Bower et al. 2017; Habouzit, Volonteri & Dubois 2017). This dominance of supernova feedback in low-mass galaxies has also been proven observationally (Martín-Navarro & Mezcua 2018) and could explain the low AGN fraction found in dwarfs compared to that of higher mass galaxies even when assuming a BH occupation fraction of 100 per cent independent of galaxy mass.

The AGN fraction, and its dependence on stellar mass and redshift, is expected to be dependent on bolometric AGN luminosity (e.g. see fig. 23 in Trump et al. 2015 and fig. 10 in Volonteri et al. 2016). Our results showcase such a behaviour for $z \leq 0.3$, where the AGN fraction decreases with X-ray luminosity for a given stellar mass range. At low L_{bol} (i.e. $L_{\mathrm{bol}} \to 0$) the AGN fraction can be taken as a proxy for BH occupation fraction; however, for high L_{bol} (i.e. $L_{\mathrm{bol}} > 10^{41}$ erg s^{-1}) the AGN fraction is a lower limit to the BH occupation fraction (Volonteri et al. 2016). Even for the lowest X-ray luminosity bin probed here ($3.7 \times 10^{41} \leq L_{0.5\text{–}10\,\mathrm{keV}} < 2.4 \times 10^{42}$ erg s^{-1}) and assuming a conservative bolometric correction factor $k = 5$ (i.e. in between those of AGN and stellar-mass sources; Mezcua et al. 2015), the bolometric luminosity is $L_{\mathrm{bol}} \geq 1.9 \times 10^{42}$ erg s^{-1} and thus the AGN fraction at $z \leq 0.3$ can only be taken as a very rough lower limit to the BH occupation fraction. This does not allow us to draw any firm conclusions on the formation mechanism of seed BHs in the early Universe, which is expected to be dominated by direct collapse if a low occupation fraction is found in local dwarf galaxies and by Population III stars if the occupation fraction in local dwarf galaxies is high (e.g. Volonteri, Lodato & Natarajan 2008; van Wassenhove et al. 2010; Volonteri 2010). Yet we note that a decrease of BH occupation frac-

tion with stellar mass is also expected from simulations of seed BH formation (e.g. Volonteri et al. 2008, 2016; Bellovary et al. 2011; Habouzit et al. 2017). The low AGN fraction found in dwarf galaxies and its decrease with decreasing stellar mass seem to favour the scenario in which seed BHs formed from direct collapse (see also Mezcua 2017); however, this might as well just be an effect caused by more massive BHs being easier to detect than light BHs and by the short time-scales of the AGN activity cycle.

The future X-ray mission concept *Lynx* would allow us to make a significant leap forwards in the study of IMBHs, in particular at high redshift. Future large-area surveys (at least 2 deg^2) and 2–3 orders of magnitude fainter than *Chandra* COSMOS Legacy would be not only crucial to provide samples large enough to fill the relevant parameter space (mass/luminosity/environment) but also deep enough to approach the low X-ray luminosities in which good constraints on the BH occupation fraction, and thus on the formation model of the SMBH progenitors, can be obtained. In this context, *Lynx* will be able to push the current sensitivity of *Chandra* COSMOS Legacy out $z = 2$ and to detect 5×10^5 M$_\odot$ BHs with $L_X = 10^{41}-10^{42}$ erg s^{-1} at $z = 10$. *Lynx* positional accuracy and spatial resolution will also be needed for these studies to securely associate multiwavelength data with the X-ray emission.

4 CONCLUSIONS

The presence of seed BHs at $z > 7$ was invoked in order to explain the finding of SMBHs when the Universe was only ∼0.8 Gyr old. While detecting these SMBH progenitors in the early Universe constitutes an observational challenge, those seeds that did not grow into SMBHs should be observed in low-mass galaxies at lower redshifts. When actively accreting, they can be easily detected as AGN by means of optical, IR, or X-ray searches. This has already yielded the detection of a few hundreds of AGN in local dwarf galaxies, most of them at $z < 0.5$.

In this paper, we report the discovery of 40 AGN located in dwarf galaxies ($10^7 \leq M_* \leq 3 \times 10^9$ M$_\odot$) out to $z \sim 2.4$. This constitutes the highest-redshift sample of AGN in low-mass galaxies, with 12 sources being at $z > 0.5$. Most of the host galaxies (39 out of 40) are star forming; yet, their X-ray luminosity is of one order magnitude higher than the typical X-ray luminosity of XRBs. The contribution from XRBs to the 0.5–10 keV X-ray emission is $\lesssim$16 per cent. After removing the XRB and hot ISM contribution to the X-ray emission, the AGN luminosities range $L_{0.5\text{–}10\,\mathrm{keV}} \sim 10^{39}-10^{44}$ erg s^{-1}. The brightest X-ray source is cid_1192, which is also the highest-redshift AGN in our sample ($z = 2.39$) and the new record-holder of an AGN in a dwarf galaxy. Based on the HRs, we find that 60 per cent of the sources are obscured and that the level of obscuration increases with redshift.

Using the recent scaling relation between BH and stellar mass of Reines & Volonteri (2015), we find a range of BH masses of $M_{\mathrm{BH}} \sim 10^4-7 \times 10^5$ M$_\odot$ and thus that all the AGNs are consistent with hosting IMBHs. The BH mass is $<3 \times 10^4$ M$_\odot$ for four of the AGN dwarf galaxies, which makes them the lightest IMBH candidates ever found in low-mass galaxies. One of the AGN dwarf galaxies has $M_* = 6.6 \times 10^7$ M$_\odot$ and constitutes the first detection of an AGN in a galaxy with $M_* < 10^8$ M$_\odot$. Most of the sources (38 out of 40) have Eddington ratios >1 per cent and three have VLA radio emission with flux densities above 17 mJy. Future near-IR follow-up observations are planned with the aim of constraining further the BH mass and properties of some of these extreme AGN.

Adding the new 40 AGN dwarf galaxies to the sample of X-ray undetected dwarf galaxies in the *Chandra* COSMOS-Legacy survey (Mezcua et al. 2016), we are able to derive the AGN fraction in dwarf galaxies out to $z = 0.7$ and, for the first time, down to a stellar mass range of $10^7 \leq M_* \leq 3 \times 10^9$ M$_\odot$, as well as to study with completeness its evolution with stellar mass, X-ray luminosity, and redshift. For $z \leq 0.3$, we find that the AGN fraction is 0.43 per cent for $10^9 < M_* \leq 3 \times 10^9$ M$_\odot$ and $L_{0.5\text{–}10\,\mathrm{keV}} \sim 10^{41}-10^{42}$ erg s^{-1} and that it decreases with X-ray luminosity and with decreasing stellar mass. For $L_{0.5\text{–}10\,\mathrm{keV}} \gtrsim 10^{42}$ erg s^{-1}, the AGN fraction is of 0.09 per cent and tentatively decreases with redshift (albeit large errors). This behaviour clearly differs from that observed in massive galaxies (>10^{10} M$_*$), suggesting that BH growth is quenched in dwarf galaxies.

The presence in the early Universe of heavy seed BHs formed from direct collapse of pregalactic gas disc is thought to be less common than that of light seeds formed from Population III stars (e.g. Volonteri et al. 2008; Volonteri 2010). Although the AGN fractions reported here constitute a merely lower limit to the true BH occupation fraction in local dwarf galaxies, the low values found and their decrease with decreasing stellar mass suggest that seed BHs could have formed predominantly through direct collapse. However, this finding might as well just be a reflection of heavier BHs being easier to detect than light ones. The low values of AGN fraction, specially at high redshift, are also expected in BH growth models in which seed BHs undergo short phases of super-Eddington accretion, which could also explain the low detection rate of high-z seed BHs (e.g. Pezzulli et al. 2017a,b). As suggested by Pezzulli et al. (2017b), wide-area X-ray surveys should be able to detect the progenitors of SMBHs at high redshift. We have proven that this is the case with *Chandra* COSMOS Legacy, which has allowed us to boost the detections of IMBHs from the local Universe to the epoch of the pinnacle of star formation and BH activity. Increasing the depth of this survey (e.g. to 250 ks), we would be able to detect AGN in dwarf galaxies out to $z = 0.5$ for $L_X \sim 10^{41}$ and out to $z = 1$ for $L_X > 10^{42}$, which would provide stronger constraints on BH seed formation models and allow us to better understand how SMBHs formed in the early Universe.

ACKNOWLEDGEMENTS

The authors thank J. Aird and M. Elvis for insightful discussion. This work was supported in part by NASA *Chandra* grant G05-16099X (M.M.), GO3-14150C, and GO3-14150B (F.C., S.M.).

REFERENCES

Agarwal B., Johnson J. L., Zackrisson E., Labbe I., van den Bosch F. C., Natarajan P., Khochfar S., 2016, MNRAS, 460, 4003
Aird J., Coil A. L., Georgakakis A., 2018, MNRAS, 474, 1225
Aird J. et al., 2012, ApJ, 746, 90
Anglés-Alcázar D., Faucher-Giguère C.-A., Quataert E., Hopkins P. F., Feldmann R., Torrey P., Wetzel A., Kereš D., 2017, MNRAS, 472, L109
Baldassare V. F., Reines A. E., Gallo E., Greene J. E., 2015, ApJ, 809, L14
Baldassare V. F., Reines A. E., Gallo E., Greene J. E., 2017, ApJ, 836, 20
Barth A. J., Ho L. C., Rutledge R. E., Sargent W. L. W., 2004, ApJ, 607, 90
Bellovary J., Volonteri M., Governato F., Shen S., Quinn T., Wadsley J., 2011, ApJ, 742, 13
Bentz M. C. et al., 2016, ApJ, 831, 2
Bower R. G., Schaye J., Frenk C. S., Theuns T., Schaller M., Crain R. A., McAlpine S., 2017, MNRAS, 465, 32
Brightman M., Nandra K., Salvato M., Hsu L.-T., Aird J., Rangel C., 2014, MNRAS, 443, 1999
Bromm V., Larson R. B., 2004, ARA&A, 42, 79
Brorby M., Kaaret P., Prestwich A., 2014, MNRAS, 441, 2346

Bruzual G., Charlot S., 2003, MNRAS, 344, 1000
Cash W., 1979, ApJ, 228, 939
Chakravorty S., Elvis M., Ferland G., 2014, MNRAS, 437, 740
Chary R., Elbaz D., 2001, ApJ, 556, 562
Chen C.-T. J. et al., 2017, ApJ, 837, 48
Chilingarian I. V., et al., 2018, preprint (arXiv:1805.01467)
Civano F. et al., 2012, ApJS, 201, 30
Civano F. et al., 2016, ApJ, 819, 62
Condon J. J., 1992, ARA&A, 30, 575
Cresci G., Vanzi L., Telles E., Lanzuisi G., Brusa M., Mingozzi M., Sauvage M., Johnson K., 2017, A&A, 604, A101
Daddi E. et al., 2007, ApJ, 670, 156
Dale D. A., Helou G., 2002, ApJ, 576, 159
Desroches L.-B., Greene J. E., Ho L. C., 2009, ApJ, 698, 1515
Devecchi B., Volonteri M., 2009, ApJ, 694, 302
Dong X.-B., Ho L. C., Yuan W., Wang T.-G., Fan X., Zhou H., Jiang N., 2012, ApJ, 755, 167
Donley J. L., Rieke G. H., Pérez-González P. G., Barro G., 2008, ApJ, 687, 111
Donley J. L. et al., 2012, ApJ, 748, 142
Dubois Y., Volonteri M., Silk J., Devriendt J., Slyz A., Teyssier R., 2015, MNRAS, 452, 1502
Elvis M. et al., 2009, ApJS, 184, 158
Fabbiano G., 2006, ARA&A, 44, 323
Falcke H., Körding E., Markoff S., 2004, A&A, 414, 895
Fan X. et al., 2003, AJ, 125, 1649
Farrell S. A., Webb N. A., Barret D., Godet O., Rodrigues J. M., 2009, Nature, 460, 73
Farrell S. A. et al., 2012, ApJ, 747, L13
Feldmeier A. et al., 2013, A&A, 554, A63
Ferrara A., Haardt F., Salvaterra R., 2013, MNRAS, 434, 2600
Fragos T., Lehmer B. D., Naoz S., Zezas A., Basu-Zych A., 2013, ApJ, 776, L31
Gallo E., Miller B. P., Fender R., 2012, MNRAS, 423, 590
Gallo E. et al., 2014, MNRAS, 445, 290
Gilfanov M., Grimm H.-J., Sunyaev R., 2004, MNRAS, 351, 1365
Goulding A. D. et al., 2012, ApJS, 202, 6
Greene J. E., 2012, Nature Commun., 3, 1304
Greene J. E., Ho L. C., 2004, ApJ, 610, 722
Greene J. E., Ho L. C., 2007a, ApJ, 656, 84
Greene J. E., Ho L. C., 2007b, ApJ, 670, 92
Greene J. E., Ho L. C., Ulvestad J. S., 2006, ApJ, 636, 56
Gültekin K., Cackett E. M., King A. L., Miller J. M., Pinkney J., 2014, ApJ, 788, L22
Gültekin K., Cackett E. M., Miller J. M., Di Matteo T., Markoff S., Richstone D. O., 2009, ApJ, 706, 404
Habouzit M., Volonteri M., Dubois Y., 2017, MNRAS, 468, 3935
Haggard D., Cool A. M., Heinke C. O., van der Marel R., Cohn H. N., Lugger P. M., Anderson J., 2013, ApJ, 773, L31
Hainline K. N., Reines A. E., Greene J. E., Stern D., 2016, ApJ, 832, 119
Hao H., Elvis M., Civano F., Lawrence A., 2011, ApJ, 733, 108
Hao H. et al., 2010, ApJ, 724, L59
Hasinger G., 2008, A&A, 490, 905
Heida M., Jonker P. G., Torres M. A. P., 2015, MNRAS, 454, L26
Hickox R. C., Markevitch M., 2006, ApJ, 645, 95
Hickox R. C. et al., 2009, ApJ, 696, 891
Hlavacek-Larrondo J., Fabian A. C., Edge A. C., Hogan M. T., 2012, MNRAS, 424, 224
Ho L. C., 2005, Ap&SS, 300, 219
Ho L. C., 2008, ARA&A, 46, 475
Johnson J. L., Haardt F., 2016, PASA, 33, 12
Kaaret P., Feng H., Roberts T. P., 2017, ARA&A, 55, 303
Kalberla P. M. W., Burton W. B., Hartmann D., Arnal E. M., Bajaja E., Morras R., Pöppel W. G. L., 2005, A&A, 440, 775
Karouzos M. et al., 2014, ApJ, 784, 137
Kauffmann G. et al., 2003, MNRAS, 346, 1055
Kim M., Ho L. C., Im M., 2017, ApJ, 844, L21
Kim M. et al., 2015, ApJ, 814, 8
Koliopanos F. et al., 2017, A&A, 601, A20
Kormendy J., Ho L. C., 2013, ARA&A, 51, 511
Kızıltan B., Baumgardt H., Loeb A., 2017, Nature, 542, 203
Lacy M., Petric A. O., Sajina A., Canalizo G., Storrie-Lombardi L. J., Armus L., Fadda D., Marleau F. R., 2007, AJ, 133, 186
Lacy M. et al., 2004, ApJS, 154, 166
La Franca F. et al., 2015, MNRAS, 449, 1526
Laigle C. et al., 2016, ApJS, 224, 24
Lanzuisi G. et al., 2013, MNRAS, 431, 978
Lara-López M. A. et al., 2010, A&A, 521, L53
Lehmer B. D., Alexander D. M., Bauer F. E., Brandt W. N., Goulding A. D., Jenkins L. P., Ptak A., Roberts T. P., 2010, ApJ, 724, 559
Lehmer B. D. et al., 2016, ApJ, 825, 7
Leigh N. W. C., Lützgendorf N., Geller A. M., Maccarone T. J., Heinke C., Sesana A., 2014, MNRAS, 444, 29
Lemons S. M., Reines A. E., Plotkin R. M., Gallo E., Greene J. E., 2015, ApJ, 805, 12
Li J.-T., Wang Q. D., 2013, MNRAS, 428, 2085
Liu H.-Y., Yuan W., Dong X.-B., Zhou H., Liu W.-J., 2018, ApJS, 235, 40
Lodato G., Natarajan P., 2006, MNRAS, 371, 1813
Loeb A., Rasio F. A., 1994, ApJ, 432, 52
Lützgendorf N., Kissler-Patig M., Gebhardt K., Baumgardt H., Noyola E., Jalali B., de Zeeuw P. T., Neumayer N., 2012, A&A, 542, A129
Lützgendorf N., Kissler-Patig M., Noyola E., Jalali B., de Zeeuw P. T., Gebhardt K., Baumgardt H., 2011, A&A, 533, A36
Lützgendorf N. et al., 2013, A&A, 552, A49
Maccarone T. J., Fender R. P., Tzioumis A. K., 2005, MNRAS, 356, L17
Madau P., Haardt F., Dotti M., 2014, ApJ, 784, L38
Mainieri V. et al., 2010, A&A, 514, A85
Mapelli M., 2016, MNRAS, 459, 3432
Mapelli M., Colpi M., Zampieri L., 2009, MNRAS, 395, L71
Mapelli M., Ripamonti E., Zampieri L., Colpi M., Bressan A., 2010, MNRAS, 408, 234
Mapelli M., Zampieri L., Mayer L., 2012, MNRAS, 423, 1309
Marchesi S. et al., 2016a, ApJ, 817, 34
Marchesi S. et al., 2016b, ApJ, 830, 100
Marleau F. R., Clancy D., Habas R., Bianconi M., 2017, A&A, 602, A28
Martín-Navarro I., Mezcua M., 2018, ApJ, 855, L20
Mayer L., Fiacconi D., Bonoli S., Quinn T., Roškar R., Shen S., Wadsley J., 2015, ApJ, 810, 51
Mayer L., Kazantzidis S., Escala A., Callegari S., 2010, Nature, 466, 1082
McConnell N. J., Ma C.-P., 2013, ApJ, 764, 184
McCracken H. J. et al., 2012, A&A, 544, A156
Merloni A., Heinz S., di Matteo T., 2003, MNRAS, 345, 1057
Mezcua M., 2017, Int. J. Mod. Phys. D, 26, 1730021
Mezcua M., Civano F., Fabbiano G., Miyaji T., Marchesi S., 2016, ApJ, 817, 20
Mezcua M., Farrell S. A., Gladstone J. C., Lobanov A. P., 2013a, MNRAS, 436, 1546
Mezcua M., Hlavacek-Larrondo J., Lucey J. R., Hogan M. T., Edge A. C., McNamara B. R., 2018, MNRAS, 474, 1342
Mezcua M., Lobanov A. P., 2011, Astron. Nachr., 332, 379
Mezcua M., Prieto M. A., 2014, ApJ, 787, 62
Mezcua M., Roberts T. P., Lobanov A. P., Sutton A. D., 2015, MNRAS, 448, 1893
Mezcua M., Roberts T. P., Sutton A. D., Lobanov A. P., 2013b, MNRAS, 436, 3128
Miller B. P., Gallo E., Greene J. E., Kelly B. C., Treu T., Woo J.-H., Baldassare V., 2015, ApJ, 799, 98
Mineo S., Gilfanov M., Sunyaev R., 2012a, MNRAS, 419, 2095
Mineo S., Gilfanov M., Sunyaev R., 2012b, MNRAS, 426, 1870
Mortlock D. J. et al., 2011, Nature, 474, 616
Murphy E. J. et al., 2011, ApJ, 737, 67
Natarajan P., 2014, Gen. Relativ. Gravit., 46, 1702
Nucita A. A., Manni L., De Paolis F., Giordano M., Ingrosso G., 2017, ApJ, 837, 66
Nyland K., Marvil J., Wrobel J. M., Young L. M., Zauderer B. A., 2012, ApJ, 753, 103

Onori F. et al., 2017, MNRAS, 468, L97
Pacucci F., Ferrara A., Grazian A., Fiore F., Giallongo E., Puccetti S., 2016, MNRAS, 459, 1432
Pakull M. W., Soria R., Motch C., 2010, Nature, 466, 209
Pardo K. et al., 2016, ApJ, 831, 203
Peterson B. M. et al., 2005, ApJ, 632, 799
Pezzulli E., Valiante R., Schneider R., 2016, MNRAS, 458, 3047
Pezzulli E., Volonteri M., Schneider R., Valiante R., 2017a, MNRAS, 471, 589
Pezzulli E., Valiante R., Orofino M. C., Schneider R., Gallerani S., Sbarrato T., 2017b, MNRAS, 466, 2131
Plotkin R. M., Markoff S., Kelly B. C., Körding E., Anderson S. F., 2012, MNRAS, 419, 267
Portegies Zwart S. F., Makino J., McMillan S. L. W., Hut P., 1999, A&A, 348, 117
Prestwich A. H., Tsantaki M., Zezas A., Jackson F., Roberts T. P., Foltz R., Linden T., Kalogera V., 2013, ApJ, 769, 92
Reines A. E., Comastri A., 2016, PASA, 33, e054
Reines A. E., Deller A. T., 2012, ApJ, 750, L24
Reines A. E., Greene J. E., Geha M., 2013, ApJ, 775, 116
Reines A. E., Plotkin R. M., Russell T. D., Mezcua M., Condon J. J., Sivakoff G. R., Johnson K. E., 2014, ApJ, 787, L30
Reines A. E., Sivakoff G. R., Johnson K. E., Brogan C. L., 2011, Nature, 470, 66
Reines A. E., Volonteri M., 2015, ApJ, 813, 82
Remillard R. A., McClintock J. E., 2006, ARA&A, 44, 49
Rodighiero G. et al., 2011, ApJ, 739, L40
Salvato M. et al., 2011, ApJ, 742, 61
Sartori L. F., Schawinski K., Treister E., Trakhtenbrot B., Koss M., Shirazi M., Oh K., 2015, MNRAS, 454, 3722
Satyapal S., Böker T., Mcalpine W., Gliozzi M., Abel N. P., Heckman T., 2009, ApJ, 704, 439
Satyapal S., Secrest N. J., McAlpine W., Ellison S. L., Fischer J., Rosenberg J. L., 2014, ApJ, 784, 113
Satyapal S., Vega D., Dudik R. P., Abel N. P., Heckman T., 2008, ApJ, 677, 926
Satyapal S., Vega D., Heckman T., O'Halloran B., Dudik R., 2007, ApJ, 663, L9
Schawinski K., Koss M., Berney S., Sartori L. F., 2015, MNRAS, 451, 2517
Schramm M. et al., 2013, ApJ, 773, 150
Secrest N. J. et al., 2015, ApJ, 798, 38
Shi Y., Rieke G., Donley J., Cooper M., Willmer C., Kirby E., 2008, ApJ, 688, 794
Silva L., Maiolino R., Granato G. L., 2004, MNRAS, 355, 973
Smith A., Bromm V., Loeb A., 2016, MNRAS, 460, 3143
Smole M., Micic M., Martinović N., 2015, MNRAS, 451, 1964
Smolčić V. et al., 2017, A&A, 602, A1
Sobral D., Matthee J., Darvish B., Schaerer D., Mobasher B., Röttgering H. J. A., Santos S., Hemmati S., 2015, ApJ, 808, 139
Soria R., Hau G. K. T., Pakull M. W., 2013, ApJ, 768, L22
Soria R., Long K. S., Blair W. P., Godfrey L., Kuntz K. D., Lenc E., Stockdale C., Winkler P. F., 2014, Science, 343, 1330
Stern D. et al., 2005, ApJ, 631, 163
Stern D. et al., 2012, ApJ, 753, 30
Strader J., Chomiuk L., Maccarone T. J., Miller-Jones J. C. A., Seth A. C., Heinke C. O., Sivakoff G. R., 2012, ApJ, 750, L27
Suh H. et al., 2017, ApJ, 841, 102
Sutton A. D., Roberts T. P., Walton D. J., Gladstone J. C., Scott A. E., 2012, MNRAS, 423, 1154
Swartz D. A., Soria R., Tennant A. F., 2008, ApJ, 684, 282
Swartz D. A., Soria R., Tennant A. F., Yukita M., 2011, ApJ, 741, 49
Tozzi P. et al., 2006, A&A, 451, 457
Trump J. R. et al., 2015, ApJ, 811, 26
van Wassenhove S., Volonteri M., Walker M. G., Gair J. R., 2010, MNRAS, 408, 1139
Venemans B. P. et al., 2013, ApJ, 779, 24
Volonteri M., 2010, A&AR, 18, 279
Volonteri M., 2012, Science, 337, 544
Volonteri M., Dubois Y., Pichon C., Devriendt J., 2016, MNRAS, 460, 2979
Volonteri M., Lodato G., Natarajan P., 2008, MNRAS, 383, 1079
Volonteri M., Rees M. J., 2005, ApJ, 633, 624
Walton D. J., Roberts T. P., Mateos S., Heard V., 2011, MNRAS, 416, 1844
Webb N. A., Barret D., Godet O., Servillat M., Farrell S. A., Oates S. R., 2010, ApJ, 712, L107
Webb N. A. et al., 2017, A&A, 602, A103
Webb N. et al., 2012, Science, 337, 554
Willott C. J. et al., 2007, AJ, 134, 2435
Wrobel J. M., Ho L. C., 2006, ApJ, 646, L95
Wrobel J. M., Miller-Jones J. C. A., Middleton M. J., 2016, AJ, 152, 22
Wrobel J. M., Nyland K. E., Miller-Jones J. C. A., 2015, AJ, 150, 120
Wu X.-B. et al., 2015, Nature, 518, 512
Yuan T.-T., Kewley L. J., Richard J., 2013, ApJ, 763, 9
Yuan W., Zhou H., Dou L., Dong X.-B., Fan X., Wang T.-G., 2014, ApJ, 782, 55
Zahid H. J. et al., 2014, ApJ, 792, 75
Zampieri L., Roberts T. P., 2009, MNRAS, 400, 677

This paper has been typeset from a TEX/LATEX file prepared by the author.